GEORG-AUGUST-UNIVERSITÄT
GÖTTINGEN

II. Physikalisches Institut

Cumulative Detector Studies of a Ge-Detector used for GERDA and Implementation of the First Prototype Interface of Geant4 and Garfield for the ATLAS Muon Tubes

von
Stefan Guindon

In this work, two particle physics projects were studied. The first project describes the effect of UV and IR light sources applied to a Germanium p-type semiconductor detector used in the GERDA experiment at Gran Sasso, Italy. The light source imitated scintillation of liquid Argon. Due to the low photon flux created by liquid Argon scintillation, it is shown that this would have no visible effect on such a detector. In the second project a first prototype interface between Geant4 and Garfield was implemented with the purpose to simulate an ATLAS muon tube, which is located at CERN in Geneva, Switzerland. Geant4 simulations allow a detector construction and the link to Garfield allows the simulation of drift paramaters from the ionization of gas detectors, which would otherwise not be possible. This is done to calculate drift properties of ionization electrons and the resulting signal in the muon tube.

Post address:
Friedrich-Hund-Platz 1
37077 Göttingen
Germany

II. Physikalisches Institut
Georg-August-Universität Göttingen
1. September 2008

GEORG-AUGUST-UNIVERSITÄT

GÖTTINGEN

II. Physikalisches Institut

Detector Studies of Photon Effect due to Liquid Argon Scintillation on a ^{76}Ge detector used for GERDA and creation of the first prototype interface of Geant4 and Garfield for ATLAS Muon Tube Analysis

von

Stefan Guindon

Dieser Forschungsbericht wurde als Diplomarbeit von der Fakultät für Physik der Georg-August-Universität zu Göttingen angenommen.

Angenommen am:	1. September 2008
Referent:	Prof. Dr. Arnulf Quadt
Korreferent:	Prof. Dr. Markus Klute

II.Physik-UniGö-Dipl-2008/05

Contents

1 Introduction **1**

2 Aspects of the Standard Model of Particle Physics **3**
2.1 The Standard Model of Particle Physics . . . 3
2.2 Neutrino Physics . . . 4
2.2.1 Neutrino Oscillations . . . 5
2.2.2 Solar Neutrino Measurements . . . 5
2.2.3 Mathematical description of Neutrino Oscillations . . . 6
2.2.4 Experimental Neutrino Results . . . 7
2.2.5 Measurements of the Neutrino Masses . . . 8
2.2.6 Neutrino Mass Hierarchy . . . 9
2.2.7 Majorana and Dirac Particles . . . 9
2.2.8 Double Beta-Decay . . . 9
2.3 Physics at Hadron Colliders . . . 11
2.3.1 Parton Distribution Functions . . . 12
2.3.2 Muon Production and Detection at Hadron Colliders . . . 13
2.3.3 Interaction of Particles with Matter . . . 13

3 Experimental Setup **17**
3.1 GERDA Experiment . . . 17
3.1.1 Overview . . . 17
3.1.2 Germanium Detectors . . . 18
3.2 Large Hadron Collider and the ATLAS Experiment . . . 19
3.2.1 LHC . . . 20
3.2.2 ATLAS Experiment . . . 21
3.2.3 Measurements at the ATLAS Detector . . . 21
3.2.4 Main Components of the ATLAS Detector . . . 23
3.2.5 Muon Ionizations inside the MDT . . . 29

4 Germanium-76 Detector Analysis **31**
4.1 Experimental Project Description . . . 31
4.2 Experimental Setup . . . 31
4.2.1 Setup of the Test Stand . . . 32
4.3 LED Light Properties and Calibration . . . 33
4.3.1 LED Light Properties at Room Temperature and in Liquid Argon . . . 33
4.3.2 LED Temperature Dependence Properties . . . 35
4.4 Analysis of Ge-76 Detector's Reaction to Photons Produced by LEDs . . . 36
4.4.1 Leakage Current produced by LEDs . . . 36
4.4.2 Measuring the Photon Flux Hitting the Detector . . . 39
4.5 Resolution of ^{60}Co Spectra when UV Light is put into Dewar . . . 40
4.6 Conclusion . . . 48

5 Muon Tube Analysis **49**
5.1 Geant4 Simulations 49
5.2 Garfield Simulations 51
5.3 Interfacing the Simulation Programs 51
5.4 Muon Tube Set-up and Run Action in Geant4 using Physical Applications from Garfield 53
5.4.1 Detector Construction 53
5.4.2 Gas in Detector 54
5.4.3 Run Action 55
5.5 Muon Tube Studies 56
5.5.1 Physics using Garfield Capabilities 57
5.5.2 Simulating the Ionizations 57
5.5.3 Calculating Drift Velocities 58
5.5.4 Calculating Drift Time 59
5.5.5 Trigger Time back to Geant4 61
5.5.6 Muon Measurements per Bunch Crossing and Timing of Interface 61
5.6 Conclusion and Outlook 62

6 Conclusion and Outlook **65**

Bibliography **67**

Acknowledgements **71**

1 Introduction

Experimental particle physics has seen many prestigious discoveries with the increase in technology for detectors. The particles interact with the detector in order to understand the physical process. These interactions inside a detector need to be studied and understood to draw conclusions on the physics of processes observed. In this thesis, a cummulative study of a neutrino physics detector and a collider physics detector is done.

The first part of this thesis, the studies of a neutrino physics detector are presented. Since the first postulation of the neutrino in 1931 by Pauli, open question have remained. These questions include the neutrino mass scale, the mass hierarchy and whether the neutrino is its own antiparticle. There are several experiments searching for the mass scale of the neutrino. However, with the observation of neutrinoless double beta-decay, all three of these questions may be answered.

The GERmanium Detector Array, GERDA, is an experiment being built to search for neutrinoless double beta-decay of ^{76}Ge. The experiment is currently set to begin operation in the near future. It is being constructed in Hall A of the Laboratori Nazionali del Gran Sasso (LNGS) in Italy. The design of the experiment was driven by the need of background suppression in order to observe a signal of neutrinoless double deta-decay.

Phase I of the experiment foresees the use of p-type ^{76}Ge semiconductor detectors. These detectors collect energy deposited from charged particles traversing through them. During the data taking, they will be submerged in liquid Argon directly. Since liquid Argon is a scintillator in the UV-range, it is uncertain as to whether or not this will effect the detectors.

To investigate the detector's performance submerged in liquid Argon, an artificial light source has been placed close to the Ge-detector. The following subjects have been studied in the first part of this thesis:

- the properties of the light sources used in the experiment;
- the effect of three different UV-wavelengths on the leakage current of the detector;
- the effect of an IR-wavelength on the leakage current of the detector;
- how the detector behaves when submerged in liquid Argon.

This investigation will help foresee any noise created by scintillation light on the detector created by the surrounding Argon. The investigation also involves the study of the wavelength properties on the resolution of a ^{60}Co source. In the end, all of the different photon fluxes are compared with the expected photon flux from liquid Argon scintillation in order to make a determination on whether Argon is a suitable candidate for the GERDA experiment.

In the second part of this thesis, studies done for a particle collider detector are presented. One such example, the LHC, will collide protons at a centre of mass energy of 14 TeV. One of the experiments at the LHC is ATLAS. An important part of the ATLAS detector is the large muon spectrometer. The spectrometer is used in order to observe muons from the collision to identify events such as Higgs Bosons or top quarks.

The muon spectrometer is made of gas tubes. To simulate the muon spectrometer, Geant4 is used. However, Geant4 is unable to study the fields and resulting ionizations in gas detectors. A secondary program, Garfield, is a simulation program used specifically for gas detectors and time projection chambers. Therefore, the second part of this thesis attempts:

- to create the first prototype interface of Geant4 with Garfield to allow the use of Geant4 to simulate gas detectors by linking all of the necessary libraries;
- to use this interface to study a muon's effect on the ATLAS muon tube, specifically the ionizations, drifting and trigger time.

Resulting from this analysis, Geant4 will have capabilities to study gas detectors, including the ATLAS muon tubes. The first protoype class called `garftube` is created which uses the physics capabilities of Garfield inside Geant4. Inside this class, the ionization and resulting drifting of electrons is measured. To complete the interface and linking of libraries, the trigger signal is returned to Geant4.

In this cumulative thesis, the detectors are studied to add an understanding of how particles interact with matter. Together, conculsions are drawn in the final section about the results found to date. Possible improvements and additions are added to this section.

2 Aspects of the Standard Model of Particle Physics

2.1 The Standard Model of Particle Physics

The Standard Model of Particle Physics (SM) is the mathematical combination of three of the four fundamental forces along with their particles [1, 2, 3]. The three fundamental forces are: electromagnetic, weak (together referred to as the electroweak) and the strong force. The fourth force, gravitation, is presently not part of the SM. Many possible extensions involve a postulation of gravity mediating particles known as gravitons.

The SM contains two sets of particles known as quarks and leptons, along with their associative antiparticles. The quarks and leptons can be divided into three generations each. Each of the three generations contains a pair of weak isospin partners. The fermions have weak isospin of $+1/2$ and $-1/2$.

The fundamental particles in the SM can be arranged into two groups, quarks and leptons. Quarks combine together to form mesons and baryons. Due to a non-Abelian term in their Lagrangian, they are subject to two properties of the strong force, confinement and asymptotic freedom. This means that quarks interact stronger at distances which are large. This results in quarks being confined to groups of quarks, and does not allow the existance of free quarks.

The quarks are: the up quark (u), down quark (d), charm quark (c), strange quark (s), top quark (t) and finally the bottom quark (b). The leptons are: the electron neutrino (ν_e), the electron (e), the muon neutrino (ν_μ), the muon (μ), the tau neutrino (ν_τ), and the tau (τ). They can be arranged as follows:

$$\begin{array}{lccc} \text{Quarks:} & \begin{pmatrix} \text{u} \\ \text{d} \end{pmatrix} & \begin{pmatrix} \text{c} \\ \text{s} \end{pmatrix} & \begin{pmatrix} \text{t} \\ \text{b} \end{pmatrix} \\ \text{Leptons:} & \begin{pmatrix} \nu_e \\ \text{e} \end{pmatrix} & \begin{pmatrix} \nu_\mu \\ \mu \end{pmatrix} & \begin{pmatrix} \nu_\tau \\ \tau \end{pmatrix} \end{array}$$

The particles' interactions are mediated by force carriers known as gauge bosons. These interactions are described by quantum field theory. The photon carries the electromagnetic force. The heavy gauge bosons are force carriers which contain mass. These are the $\text{W}^\pm$ and Z^0 which carry the weak force. The final force carrier in the SM is the gluon. There are eight different gluons which carry the strong force and bind nuclei together. The forces along with their properties are shown in Tab. 2.1.

Force	Relative Strength	Gauge Boson	Theory
Strong	1	8 gluons	QCD
Electronmagnetic	10^{-2}	γ	QED
Weak	10^{-6}	$W^{\pm}$	QFD
Gravitation	$< 10^{-40}$	Gravitons	General Theory of Relativity

Table 2.1: Overview of the four known forces along with their properties. Gravitational force is added to show a comparison of all fundamental forces, even though the graviton has yet to be observed, and is currently not part of the SM.

In addition, the SM contains the Higgs Boson [4, 5]. The Higgs Mechanism is the theoretical description which allows certain particles have mass and others not. The Higgs Boson is the only particle in the SM which has not yet been observed.

However, the SM is not complete to describe the universe. There are still open questions in many of the aspects of the model. A few of the open questions are:

- Why is there more matter than antimatter in our present day universe? If it is believed that the Big Bang produced equal amounts of each, then it is hard to imagine how the annihilation of mostly all the matter resulted in a tiny fraction of matter remaining. It is still uncertain whether charge-parity (CP) violations in the Standard Model are enough to describe this asymmetry.

- Why are the strengths of the fundamental forces so different from one another? On some scale, it might be possible for all of the four forces, including gravity, to meet to form a Grand Unified Theory (GUT). This would be similar to the already combined weak and electromagnetic forces into the electroweak force.

- Why is the universe composed of dark matter, matter which can only be detected through gravity? What is the composition of dark matter and dark energy which make up most of our universe, 73 % dark energy and 23 % dark matter. This question is being sought by supersymmetric theories, in which neutral, low mass supersymmetric particles are predicted. These are good candidates for dark matter.

These questions which are left open by the Standard Model are the driving mechanism for modern experiments such as the LHC at CERN, which searches for the Higgs Boson, CP violation and possible dark matter candidates.

The one type of particle in the SM which scientists still know little about is the neutrino. This neutrino, which has three flavours, is a very weakly interacting particle which is almost undetectable. This makes the neutrino a particle which continues to be sought after in experiments such as GERDA.

2.2 Neutrino Physics

The neutrino has a history which dates back to 1930, at which point a problem had presented itself in nuclear beta-decay. Beta-decay occurs when a heavier nucleus decays into a lighter one,

with the emission of an electron, termed the beta particle.

$$A \rightarrow B + e^{-}. \tag{2.1}$$

The problem with the understanding of the decay at the time was that in the centre of mass frame, as in all frames, energy is conserved. If particle A decays into particle B, which both have fixed masses, along with the electrons fixed mass, the electron energy is expected to be fixed. However when the experiments were carried out, it was shown that in fact the electron did not have a fixed energy from the beta-decay, but a continuous spectrum of energy. At the time, this was extremely surprising and provoked many physicists to postulate whether or not energy is conserved.

It took two years for Pauli to propose a new light particle which took the missing energy from the interaction, which only interacted via the weak force. This was met with skepticism from the physics community and it was not until the late 1940s that it was theoretically accepted as an explanation for the broad emission of electron energies in beta-decay. The problem still was the lack of theoretical evidence for the particle we now know as the neutrino.

Detection of the neutrino is difficult due to the fact that it is only interacting via the weak interaction. It was not until the 1950's when neutrinos were detected for the first time. Today, with elaborate experiments it is known that there are three generations of neutrinos, the last of which, the tau neutrino, was discovered in 2000.

2.2.1 Neutrino Oscillations

Early on, it was thought that the neutrino mass was zero. This was found not to be the case in 1998 at Kamiokande when the flux of solar electron neutrinos was found to be different here on Earth as compared to that of the expected flux emitted from the Sun. These measurements were done by SNO in Sudbury, Canada. Since neutrinos weakly interact with matter, there was very little to explain why the number of neutrinos observed on earth was different from that expected to be emitted by the sun.

To explain this anomaly, scientists came to the conclusion that neutrinos emitted from the sun oscillate, meaning they change between the three flavours during their flight. This explained the discrepancy in observed electron neutrinos here on earth: they had oscillated into other flavours.

2.2.2 Solar Neutrino Measurements

The first neutrino experiments were done using the most well known abundant source of neutrinos, the sun [6]. The original solar neutrino experiment to measure the solar neutrino flux was at the Homestake gold mine in 1968 [7]. They measured the electron neutrino flux to be $(2.56 \pm 0.16 \pm 0.16)$ SNU, where SNU is the Solar Neutrino Unit. It is defined as 10^{-36} captures/(atom·s).

The value of the solar neutrino flux as predicted by the Standard Solar Model at the time was (8.1 ± 1.3) SNU. A spectrum of neutrino energies is shown in Fig. 2.1. The value found by the group at Homestake was significantly lower than the predicted value. Therefore other experiments such as GALLEX [8], GNO [9] and SAGE [10] were conducted in similar manners

in order to confirm or refute the experimental value. Both experiments showed the same large deviation from the predicted value as was found originally at Homestake.

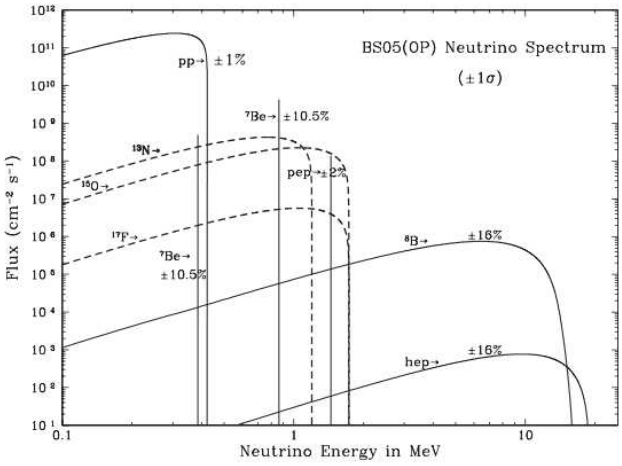

Figure 2.1: Flux of solar neutrinos as a function of their energy as predicted by the Standard Solar Model BS05(0P).

It was not until later that large scale detectors were built to observe this flux with greater precision and understanding. Kamiokande [11], and later Super-Kamiokande [12], were able to observe not only the flux of neutrinos, but were also able to show due to Cherenkov light, the direction of incoming neutrinos. Kamiokande was able to show for the first time in experiment that the measured neutrinos come from the sun. However, the flux was again lower than the Standard Solar Model predicted.

The final piece in the puzzle of the solar neutrino flux was added at the Sudbury Neutrino Observatory, SNO in Sudbury, Canada [13]. Using heavy water (D_2O) as its target, it was able to measure all flavours of neutrinos, not just the flux of electron neutrinos. When the flux of all the flavours were measured it was seen that the solar neutrinos, which are electron neutrinos when they leave the sun, transition into muon and tau neutrinos on the way to the earth where they are detected. This is interpreted to be the reason for such small electron neutrino flux seen on earth. This was a new interpretation of particle behaviour at the turn of the last century which led to the first description of neutrino oscillations. A similar mechanism has been observed in the quark sector (CKM-Matrix). Raymond Davis, Jr. and Masatoshi Koshiba were awarded the Nobel Prize in Physics in the year 2002 for their contribution on the detection of solar neutrinos.

2.2.3 Mathematical description of Neutrino Oscillations

To describe neutrino oscillations, one can describe the neutrinos in terms of mass eigenstates ν_j(j= $1, 2, 3$) and flavour eigenstates $\nu_\alpha(\alpha = 1, 2, 3)$. In general, mass eigenstates and flavour eigenstates are not the same. In fact, the flavour eigenstates are a combination of the mass eigenstates:

$$|\nu_\alpha > \ = \sum_j U^*_{\alpha j} |\nu_j > \ , \tag{2.2}$$

where U is the unitary Pontecorvo-Maki-Nakagawa-Sakata (PMNS) matrix. For three generations of neutrinos it has three angles and one CP-violating phase (three if the neutrino is its own antiparticle).

The time evolution of a neutrino over a distance L can be calculated using Schrödinger's equation. This yields

$$|\nu_\alpha(L)> \approx \sum_j U^*_{\alpha j} e^{-i(m_j^2/2E)L} |\nu_j> \ , \tag{2.3}$$

where m_j is the mass of the jth mass eigenstate and E is the average energy of the mass eigenstates. The transition probability from a state α to a state β over a distance L is $|<\nu_\beta|\nu_\alpha(L)>|^2$ and can be calculated using:

$$|\nu_\alpha(L)> \approx \sum_\beta \left[\sum_j U^*_{\alpha j} e^{-i(m_j^2/2E)L} \right] U_{\beta j} |\nu_\beta> \ , \tag{2.4}$$

which results in the probability to transition from one state to another:

$$P_{\alpha\to\beta} \propto \sin^2\left(\frac{\Delta m^2 L}{4E}\right) \ . \tag{2.5}$$

where E is the energy and $\Delta m^2 = m_j^2 - m_i^2$ is the difference between the masses squared of the two neutrinos.

From the derivation of the probability of flavour oscillations, it can be seen that flavour oscillations are only possible if at least one neutrino has a finite mass. However, it can also be seen that neutrino oscillations are only sensitive to mass differences, not to the absolute scale of neutrino masses.

2.2.4 Experimental Neutrino Results

From the description of neutrino oscillations, it was understood that neutrinos had mass. However, there are still problems which need to be solved in neutrino physics. These open questions are:

- The absolute mass of the neutrinos. The masses of the neutrinos are now believed to be finite and non-zero with the mathematical description of neutrino oscillations, however of a very tiny fraction. Therefore there is a continuing search to find the mass of the neutrinos.
- The mass hierarchy of the neutrinos. From the description of neutrino oscillations, specifically the mass difference squared (Δm^2), it is uncertain as to whether neutrinos from the sun or from the atmosphere are the heaviest. This is due to the fact that Δm can be positive or negative.
- The nature of the neutrinos. It is still undetermined as to the nature of the neutrino: Majorana or Dirac. The neutrino could be its own antiparticle, Majorana, or it could have separate particle and antiparticle, in which case it is called a Dirac particle. If it is discovered that the neutrino is Majorana, it would be the first known fermion to be of this nature.

These three open questions in neutrino physics will be discussed in the following sections.

2.2.5 Measurements of the Neutrino Masses

Neutrino masses cannot be directly measured. They can be indirectly measured in reactions containing neutrinos of a specific flavour. The mass of a flavour eigenstate is defined as the incoherent sum of the masses of the mass eigenstates:

$$< m_{\nu_\alpha} > \; = \sqrt{\sum_i |U_{\alpha i}|^2 m_i^2} \; , \tag{2.6}$$

where U is again the PMNS matrix.

Measurements of the electron neutrino mass can be done using the energy spectrum of the electron in beta-decays. The electron energies range almost up to the Q-value of the decay. The Q-value is the total energy released in a decay. The mass of the neutrino kinematically defines the endpoint of the energy spectrum. This can be seen in Fig. 2.2.

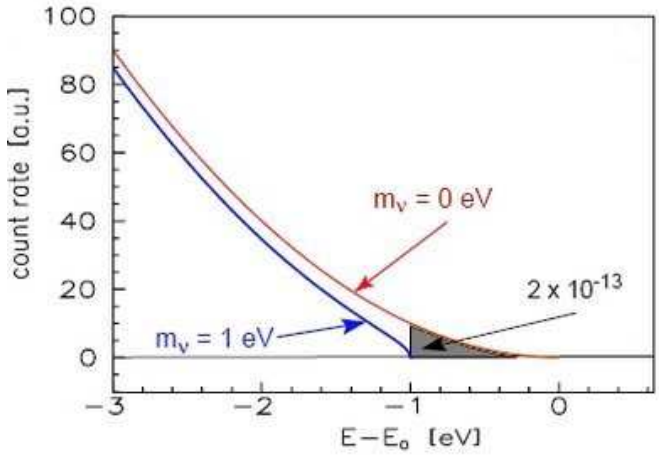

Figure 2.2: The relative electron energy spectrum from beta decay with different masses of the neutrino. For a massive neutrino, the tail is cut short of the full spectrum

Recent experiments such as Mainz [14] and Troitsk [15] use tritium beta-decays and were able to set the limit of $m_{\nu_e} < 2.3$ eV (95 % C.L.). The next generation is the KATRIN experiment [16] in Karlsruhe, Germany, where a large spectrometer is being used to measure the electron momentum with such precision that the electron neutrino mass can be measured down to about 200 meV.

The muon neutrino mass can be measured by positive pions decaying into a positively charged muons and muon neutrinos. The decay is:

$$\pi^+ \rightarrow \mu^+ \nu_\mu \; . \tag{2.7}$$

From the measurements of the pion mass, muon mass, and muon momentum, one is able to calculate the muon neutrino mass as:

$$< m_{\nu_\mu} > \; = \sqrt{m_\pi^2 + m_\mu^2 - 2m_\pi \sqrt{p_\mu^2 + m_\mu^2}} \; . \tag{2.8}$$

To date, the limit on the muon neutrino mass is $m_{\nu_\mu} < 170$ keV (90 % C.L.). Future experiments such as NuMass will hopefully be able to measure the muon mass down to 8 keV [17].

The tau neutrino mass is determined by tau decays, much like the muon decays. It is done in e^+e^- colliders such as LEP at CERN. To date, an upper bound on the tau neutrino mass is set at $m_{\nu_\tau} < 18.2$ MeV (95 % C.L.).

2.2.6 Neutrino Mass Hierarchy

From the measurements of neutrino oscillations, the difference between neutrino masses can be measured. However, it is uncertain from these measurements whether the atmospheric or solar neutrinos are the heavier. It is obvious from Eq. (2.5) that the sign of Δm^2 cannot be measured with neutrino oscillations. This leads to two different hierarchies of neutrino masses, normal or inverted, as seen in Fig. 2.3. From neutrino oscillations in matter, the sign of Δm^2_{21} can be measured. It is the sign of Δm^2_{32} which to date has not been measured.

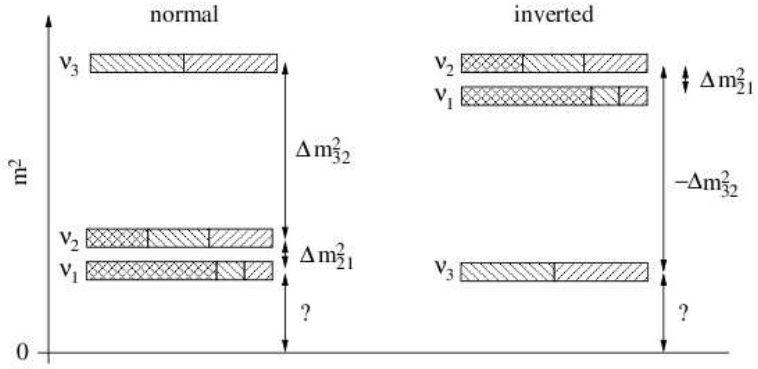

Figure 2.3: Two different mass hierarchies of the neutrino. It is uncertain which scale is realized in nature.

2.2.7 Majorana and Dirac Particles

The introduction of the neutrino also brought questions about its nature. It is still not understood whether or not the neutrino is also its own antiparticle. If the neutrino is its own antiparticle, it is called a "Majorana" neutrino. If it is not, it is called a "Dirac" neutrino. Today, the only experimentally feasible process to measure the nature of the neutrino is neutrinoless double beta-decay ($0\nu\beta\beta$).

2.2.8 Double Beta-Decay

Double beta-decay occurs in a nucleus when two of the neutrons decay into protons with the release of two electrons and two antineutrinos. It is a weakly occuring process as it is a second order weak decay. The process may occur via two modes: two neutrino double beta-decay ($2\nu\beta\beta$) or neutrinoless double beta-decay ($0\nu\beta\beta$). The decays can be written as and can

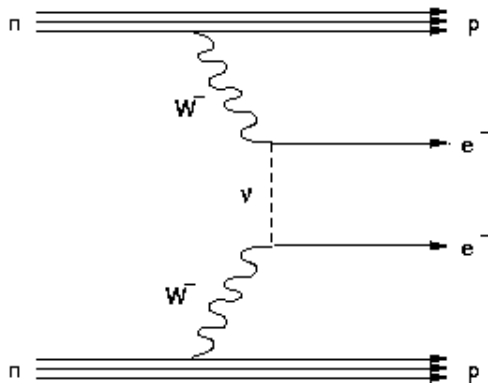

Figure 2.4: Feynmann diagram for neutrinoless double beta-decay.

be shown with Feynman diagrams in Fig. 2.5 (left):

$$2\nu\beta\beta: \ (Z,A) \ \rightarrow \ (Z+2,A) + 2e^- + 2\bar{\nu}_e \ , \tag{2.9}$$

$$0\nu\beta\beta: \ (Z,A) \ \rightarrow \ (Z+2,A) + 2e^- \ . \tag{2.10}$$

$2\nu\beta\beta$-decay occurs when two neutrons decay into protons inside the nucleus, releasing two electrons and two antineutrinos. When measuring the electrons' energy of this decay, it is a continuous spectrum. This is due to the total energy, Q-value, being shared by all four leptons in the decay. This is shown in Fig. 2.5 (right). This process also conserves lepton number, both sides of the equation having a lepton number of 0. This process is also observed in experiments of different nuclei.

$0\nu\beta\beta$-decay is a possible decay process if the neutrino has Majorana nature and the two neutrinos are to annihilate with one another during the double beta-decay. It has yet to be seen experimentally. If this process is to be realized, the total energy from the decay, Q-value, would be shared only by the electrons. This results in a sharp peak in the energy spectrum at the Q-value which is given to the two electrons. This is shown in Fig. 2.5 (right). This process also does not conserve lepton number, as the initial state has a lepton number of 0 and the final state +2. The observation of $0\nu\beta\beta$-decay would show that the neutrino has Majorana nature.

To search for a candidate for double beta-decay, the parent nucleus must have a forbidden single beta-deacy. In other words, the daughter nucleus must have a heavier nucleus than the parent. Another requirement is that the parent nucleus must be heavier than the double beta-decay daughter nucleus. This decay is possible in ^{76}Ge. To show this, the isobars of $A = 76$ are shown in Fig. 2.6.

This makes ^{76}Ge a good candidate search for neutrinoless double beta-decay. This process would result in a decay as follows:

$$^{76}Ge \rightarrow^{76} Se + 2e^- \ . \tag{2.11}$$

If this process were to occur, it would show the nature of the neutrino to be Majorana and further the belief that neutrinos have mass. The choice of using ^{76}Ge for the search of $0\nu\beta\beta$ has been done in the GERDA experiment.

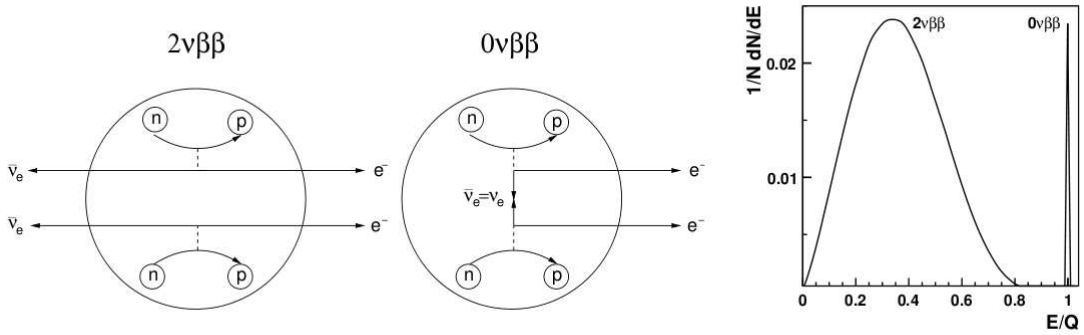

Figure 2.5: (Left): The two possible decay channels for double beta-decay, either by emitting two neutrinos $2\nu\beta\beta$ or by emitting zero neutrinos $0\nu\beta\beta$. It can clearly be seen how lepton number is violated if the neutrino is Majorana, as is the case in $0\nu\beta\beta$. (Right): Energy spectrum from the two double beta-decays. The graph is normalized to the Q-value.

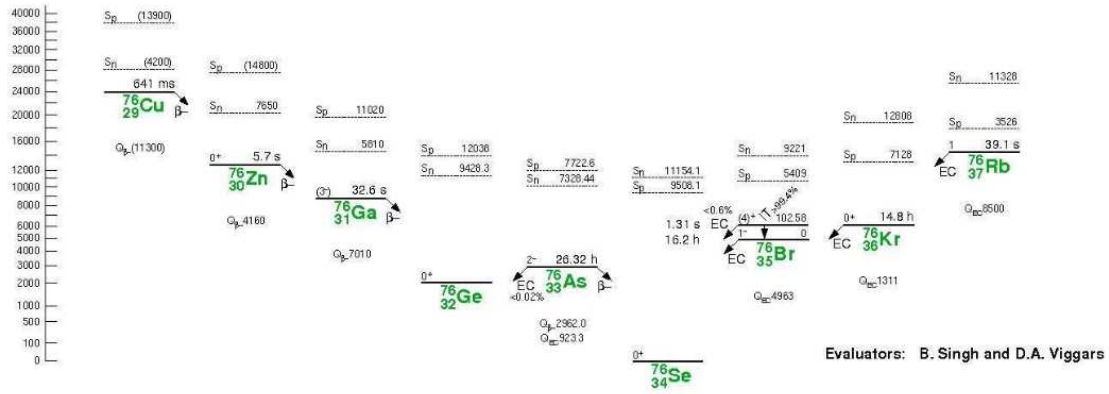

Figure 2.6: Isobars for $A = 76$. Double beta-decay can occur in ^{76}Ge due to the forbidden single beta-decay to ^{76}As due to its larger binding energy. However the double beta-decay is allowed to ^{76}Se since its binding energy is lower than ^{76}Ge.

2.3 Physics at Hadron Colliders

Hadron colliders differ from neutrino experiments due to the dynamics and physical processes which occur. The hadron colliders collide two hadrons together in the hope of creating new particles from the interaction. The Tevatron at Fermilab in Chicago, USA, collides protons and antiprotons at a centre of mass energy of 1.96 TeV. It has been in operation since 1987 and will continue until 2009 or 2010. The Large Hadron Collider (LHC) at CERN will collide protons together at higher centre of mass energies, up to 14 TeV. The LHC will begin operation in late 2008.

Hadrons, such as protons, are composed of quarks and gluons. For the proton, it is composed of two up and one down valence quark, along with the gluons carrying the force between them. These gluons can create quark - anti-quark pairs known as sea quarks inside the proton. This

makes the proton a mix of valence quarks, sea quarks and gluons. To our present day knowledge, quarks do not contain sub-structure, meaning they are the fundamental particles interacting in hadron colliders. Therefore, to describe events at hadron colliders, the interactions of the quarks and gluons, along with the structure of the proton, must be understood.

The fundamental interaction of the quarks is Quantum Chromodynamics (QCD), which describes the interaction of the strong force. The force is mediated by eight gluons which make up the strong interaction. This interaction, as stated before holds the protons and other baryons and mesons together with its properties from the non-Abelian term in the Lagrangian.

2.3.1 Parton Distribution Functions

To describe the proton, in a proton - proton collision, the parton model is used. The parton model was developed to describe the proton structure. The parton model describes the momentum fraction, x, distributed to the proton constituents.

The proton itself is comprised of partons, quarks and gluons. If the proton was only comprised of one parton, this one parton would contain the full proton momentum. Hence, the parton distribution of momentum would be a delta function at $x = 1$. If the proton is composed of just three valence quarks, two up quarks and one down, the parton distribution would again be a delta function at $x = 1/3$. This would represent three quarks carrying each $1/3$ of the proton momentum. If energy is added to the system, then these valence quarks would interact via gluons, which would in turn create quark - antiquark pairs known as sea quarks. This would cause a large fraction of sea quarks and gluons carrying a low fraction of the proton's momentum.

One of the locations where the parton model was studied was at DESY in Hamburg, Germany. There, the parton density function of the proton was measured. It is shown in Fig. 2.7. From the figure, the composition of the proton can be seen at different fractions of the momentum. As the proton is probed at higher energies, the lower momentum regions are analyzed.

Therefore when studying the events in Hadron colliders, the distribution of the quarks and gluons inside the protons must be understood in order to determine from which process the event was created. At high energies in the LHC, the protons will contain many different sea quarks and gluons along with their three valence quarks. The interactions may come from, e.g., quark - anti-quark annihilations or from gluon fusion processes which occur in the interaction of partons. This makes the hadron collider a complex physical interaction in which the initial properties of the collision are not fully known to scientists describing the event afterwards.

At colliders, there are many SM and beyond SM processes which are studied. Some of these processes include:

- the study of top quark,
- the search for the Higgs Boson,
- the study of possible additions to the SM in the form of supersymmetric particles (SUSY).

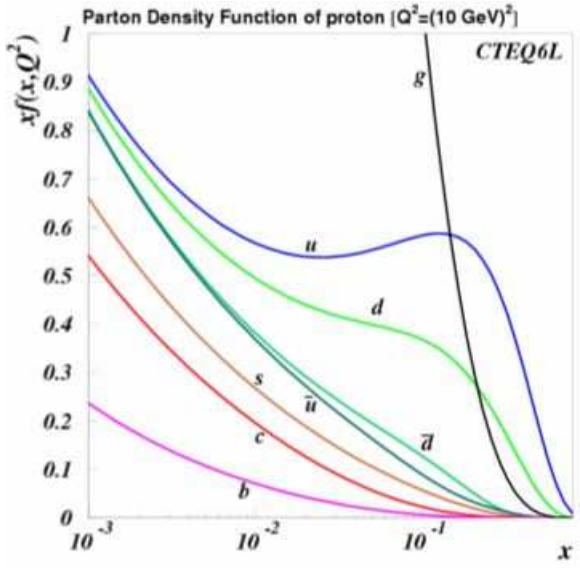

Figure 2.7: Parton density function of a proton [18]. This shows the momentum distribution of all the partons inside of the proton with different momentum fractions x. As the energy of the proton increases, the energy can be shared by many low momentum partons at low x.

The key to observing these processes in hadron colliders is through the understanding of their decay products and interactions with the detector. For the study of the top quark and Higgs Boson, possible decay channels foresee the production of muons which can easily be tagged in hadron colliders. Therefore it is important to understand the muon and how it interacts with the hadron collider detector in order to study the SM and possible physics beyond the SM.

2.3.2 Muon Production and Detection at Hadron Colliders

The identification of muons in hadron colliders is essential to distinguish it from other particles. Muons are produced in hadron colliders from a vast amount of processes. Some of which are the Higgs Boson decay and top quark decay. Muons are also created from decay of pions. From this decay, many muons contain a momentum of approximately 0.1 to 10 GeV/c. At this energy, the muon is a minimum ionizing particle. This is described by the Bethe-Bloch equation [19]. This can be seen in Fig. 2.8.

Muons created at 1-10 GeV of energy are created primarily from pions. Pions are created usually in a jet, a cone of hadrons and leptons moving in one direction. They then decay inside the detector into muons. These muons deposit a tiny fraction of their energy in the detector, as they are minimum ionizing particles. Therefore they can escape the detector. As a result, to detect muons, an additional muon spectrometer is added to the exterior of the experiment. This allows muon identification in hadron colliders.

2.3.3 Interaction of Particles with Matter

When a charged particle passes through a gas detector, it is the interaction of the charged particle with the gas which is measured. For a charged particle such as a muon, the detection is through the ionization of a gas detector. As the muon passes through the gas detector, it

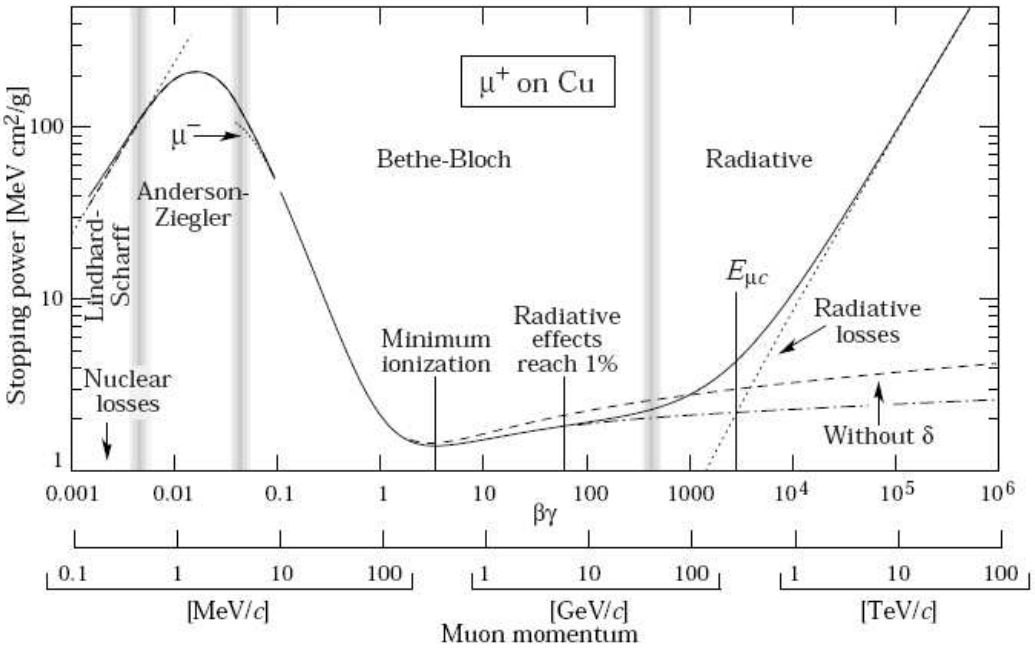

Figure 2.8: Average stopping power of muons on Copper taken from [20, 21]. This shows the different amounts energy a muon loses, and by what means, as a function of its momentum. When a muon has a momentum in the range of 1 GeV/c it is considered a minimum ionizing particle. This means that it loses a minimum amount of energy in material at this momentum.

interacts with the atoms of the gas. The muon passes by the gas atom, Argon in the case of the ATLAS muon tubes, and gives its energy to an electron in the atom. This electron then is emitted from the atom and is free to drift according to the electric field in the tube.

In addition to the ionization of the gas due to a passing charged particle, the interaction between the particle and gas can also create multiple scatterings. Multiple scatterings are the result of many small elastic Coulomb scatterings. Coulomb scatterings result in a particle's change in direction. Classically, it is the result of the muon passing by the Argon nucleus and experiencing a strong electric field. As a result, the muon's trajectory is changed significantly. The addition of many of these scatterings can result in a very pronounced deviation.

When taking into account the effects of ionization, there is a profound effect in the high energy transfer to atoms. This effect was first calculated by physicist Landau in 1944. The distribution of energy loss by a charged particle is described by the Landau distribution which has a long tail at higher energy transfers.

The Landau peak describes the energy transfer for a charged particle. When the mean energy loss is very low, in the case of our muons in the Argon gas, there can occur high energy

transfer interactions. These high energy interactions create what is referred to as a "delta-electron". This electron has high enough energy to create its own ionization and deposit signals inside gas detectors. The energy transfer by charged particles is shown in Fig. 2.9.

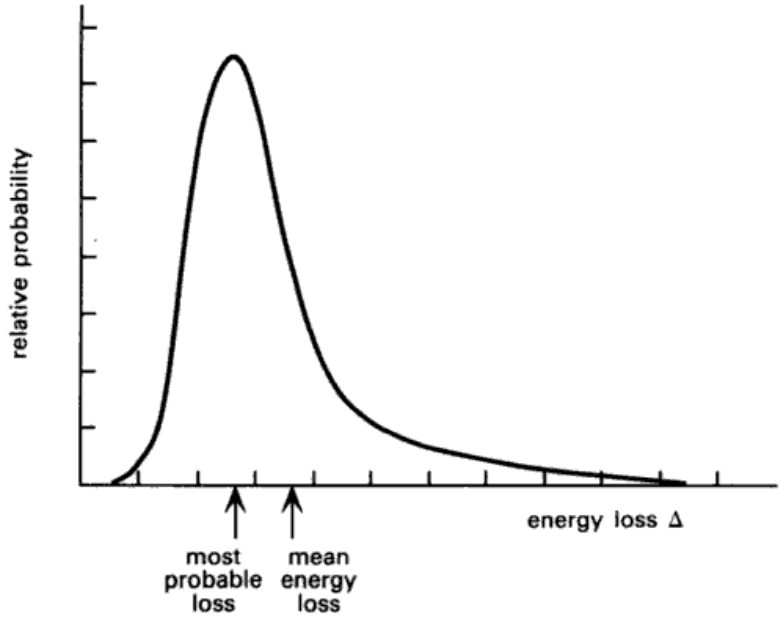

Figure 2.9: Landau distribution which describes closely the energy deposition of charged particles. The peak is approximately Gaussian, however with a mean at higher energies than the most probable energy loss. This is due to the long tail from the production of "delta-electrons".

Ionization in the detector is the primary method of calculating signals of charged particles. Once the electrons have been created they are subject to the electric field and drift accordingly. The process is affected by diffusion and avalanche creations. An avalanche occurs as the electrons reach a high electric field when close to the wire. They create an increasing amount of particles as they arrive at the wire. This signal is detected by the build-up of the charged electrons, and is used as the method of determining whether a charged particle has entered the gas detector. The combination of these electrons along with the drifting ions creates the signal in a muon tube.

3 Experimental Setup

The experimental setup of the detectors is the key to understanding the physics at experiments. In this section, the first detector described is the detector of the GERDA experiment. The use and construction of the detector array is shown in order to provide an understanding into whether liquid Argon is a suitable candidate for the detector construction.

The second detector described in this section is the ATLAS detector at the LHC. Emphasis is placed on the muon spectrometer since muons which escape the inner detector and calorimeter can be detected by gas tubes.

3.1 GERDA Experiment

3.1.1 Overview

The Germanium Detector Array, GERDA [22], is a neutrino experiment which is currently being built at Laboratori Nazionali del Gran Sasso (LNGS), Italy. It will search for neutrinoless double beta-decay in ^{76}Ge. Data taking will start in the near future.

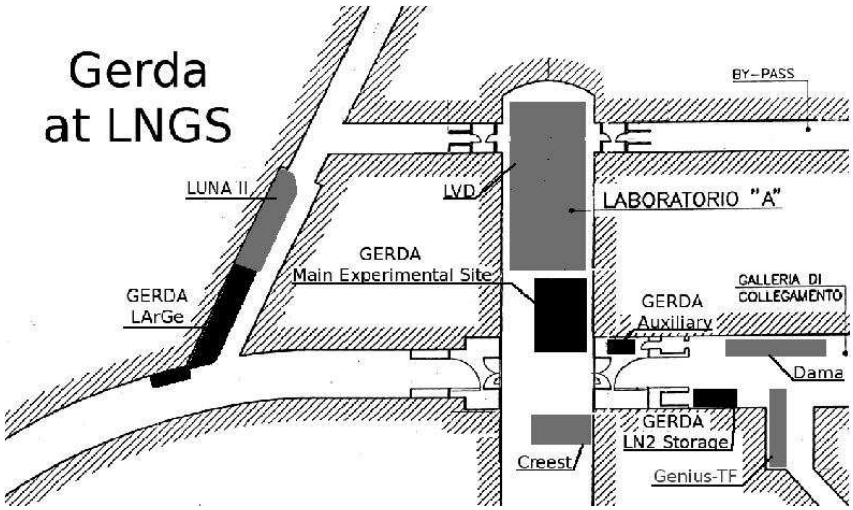

Figure 3.1: Floor plan of the LNGS near Rome, Italy, with its underground caverns. The GERDA experiment is being constructed in Hall A of the Laboratory.

As $0\nu\beta\beta$ is a rare process, the identification of signal and background processes is very important. The background / signal ratio needs to be kept to a minimum in order to observe a signal. Therefore the design of the experiment is driven by the need to shield sources of background. The main features of the GERDA design are:

- The use of submerged detectors into liquid Argon. This, along with the use of low Z materials helps to keep the detector at a distance from radiation of materials used in the design.

- The construction of the experiment underground. This will help shield the detector from cosmic radiation, in particular cosmic muons which would leave a signal in the detector.

- The construction of a shell-like shielding. The tank housing the detector is a copper lined steel vessel. It is kept in a layer of ultra-pure water. On the top of the tank is the clean room which contains plastic scintillator plates just above it. All of these mechanisms will help shield the germanium crystals from unwanted cosmic muons and radioactive sources.

Another interesting feature of the design is the use of photomultipliers in the water surrounding the tank. This will help to determine if a muon entered the tank and deposited a signal in the detector. This will help to distinguish a potential $0\nu\beta\beta$ signal from a cosmic muon. The GERDA assembly is shown in Fig. 3.2.

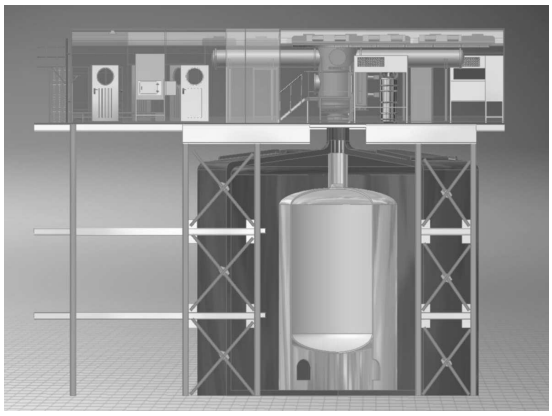

Figure 3.2: A side view of the GERDA assembly. The large dewar holds the detector suspended in liquid argon. The clean room sits on top of the experiment.

3.1.2 Germanium Detectors

The germanium detectors are semiconductors. A reverse bias voltage creates a depleted zone. Energy deposited in the depletion zone by a charged particle will create electron - hole (e^-/h) pairs. Due to the applied electric field created by the reverse bias voltage, the e^- and h will drift towards the electrode and outer surface. The number of e^-/h pairs created is directly proportional to the energy deposited by the charged particle. This makes it possible to make a determination of the energy of the original particle.

The germanium detectors play the most important role in the GERDA experiment. The detectors are arranged in a hexagonal array. The array will eventually in future phases be up to five layers, vertically stacked on top of one another. In each layer, there can be up to 19 detectors. The design and experiment is divided into Phase I and Phase II, where Phase II will add more detectors and better background suppression for a more complete analysis.

The center of the detectors in one layer are separated by a space of 9 cm. The vertical distance is 5 cm. This set-up can be seen in Fig. 3.3, where a possible Phase II detector array is shown.

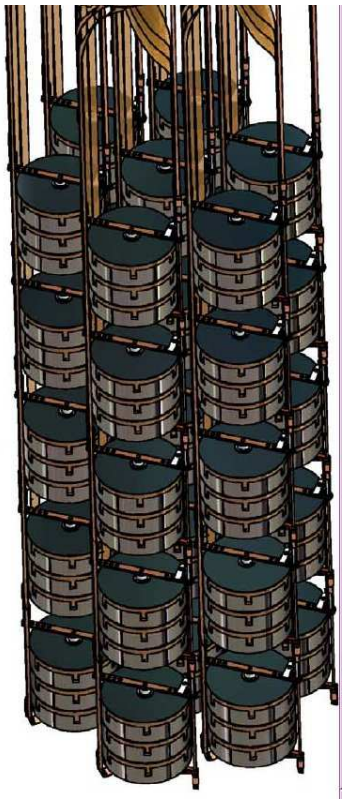

Figure 3.3: Picture showing a possible Phase II detector array with a hexagonal arrangement in five levels.

Phase I detectors will be p-type semiconductor germanium crystals. They are enriched in ^{76}Ge to a level of about 86%. Phase II detectors will be n-type semiconductors. They will be about 70 mm in height and 75 mm in diameter. The crystal has a six-fold segmentation in the azimuthal angle ϕ and a three-fold segmentation in the height. Each segment will be read out separately, as will the core electrode thus yielding 19 readout channels. This will improve the position resolution of signals and thus the signal to noise ratio. One such Phase II detector can be seen in Fig. 3.4.

3.2 Large Hadron Collider and the ATLAS Experiment

The Large Hadron Collider, LHC, will be the world's largest particle collider when it begins operation in late 2008. It will house four experiments which will study different aspects of high energy physics. One of the four experiments is the ATLAS experiment. The ATLAS experiment is searching for, among other thingss, the Higgs Boson and possible supersymmetric particles. It will also produce a large number of top and anti-top pair production, hoping to rediscover the top quark which was found in 1995 at the Tevatron.

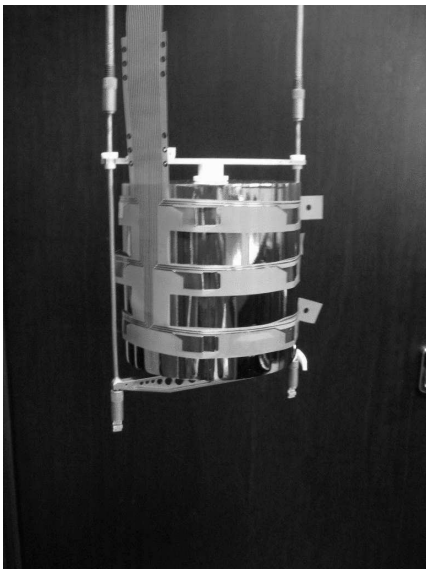

Figure 3.4: A Phase II germanium detector planned to be used for the GERDA experiment.

This is done with signal recognition and particle identification detectors. Specific focus is on the muon spectrometer for particle tracking due to the specific nature of the muon spectrometer. Since only muons deposit a signal in the muon spectrometer, it is important to identify muons for possible channels of decay, e.g., of a Higgs Boson or top quarks. Therefore, specific emphasis is placed on the muon's signal and energy deposition in the ATLAS muon spectrometer.

3.2.1 LHC

The LHC [23], is a particle collider. It is set to begin operation in autumn 2008. It is in the final stages of preparation, constructed just outside of Geneva, Switzerland, at the CERN laboratories. It is a proton - proton collider with a centre of mass energy of 14 TeV and a design luminosity of 10^{34} $\mathrm{cm}^{-2}\mathrm{s}^{-1}$. The luminosity characterizes the detector, as it describes the number of particles per unit area per unit time inside the interacting area of the particles, which is determined by the crossings per unit time. The LHC will have approximately 25 proton - proton collisions per bunch crossing.

The collider itself has a circumference of 27 km, situated on average 100 m underground. Prior to being injected into the LHC, the protons are accelerated by a system of smaller accelerators.

The protons are created first and injected into the LINAC, which is a linear accelerator. This increases the proton energy up to 50 MeV. From there they are injected into the PS Booster which again accelerates the protons to an energy of 26 GeV. Once they have reached this energy they are sent into the SPS where they accelerate to 450 GeV. This is the final section before the injection into the LHC in two opposite directions. Once the energy of 7 TeV is reached in both directions, they are collided at one of the experiments in the LHC ring.

To reach such high energies at the LHC, magnetic dipoles and correction magnetic quadropoles to keep the protons aligned in the tunnel are used. The magnets are superconducting and the

apparatus is cooled down to 1.9 K to allow for superfluid Helium.

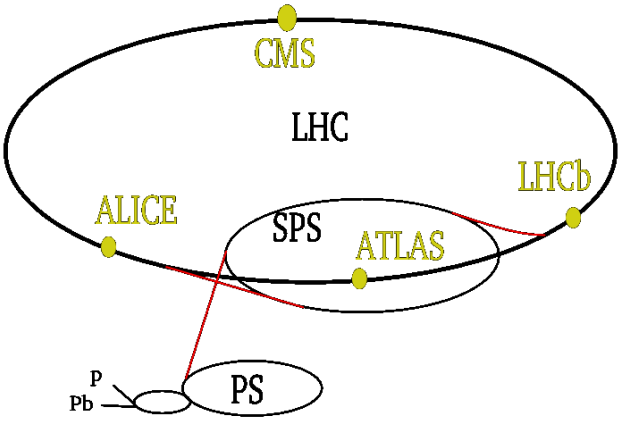

Figure 3.5: The LHC and other supporting rings which the protons will circulate to increase their energy to 7 TeV before colliding at one of the experiments along the LHC ring.

Along the LHC, there are four experiments: ALICE [24], LHCb [25], CMS [26] and ATLAS [27]. ALICE will examine the quark - gluon plasma similar to those which occurred immediately after the big bang by colliding lead ions together. LHCb searches for CP violations in the b-quark sector. CMS and ATLAS are multipurpose experiments. The physics programs include searches for the Higgs particle, supersymmetry and possible extensions to the SM, for example extra dimensions.

3.2.2 ATLAS Experiment

The ATLAS detector, (**A** **T**oroidal **L**HC **A**pparatu**S**) is a large particle detector, housed at point 1 in the LHC. It has a height of 25 m and a width of 22 m, all situated inside a cavern about 100 m under the Swiss countryside. It weighs approximately 7 000 tons. The ATLAS detector can be seen in Fig. 3.6, having a typical onion shell structure with five main components:

- the inner detector,
- the electromagnetic calorimeter,
- the hadronic calorimeter,
- the muon detectors, and
- two magnets.

The ATLAS Collaboration is the largest physics collaboration in the world. As of early 2008, 37 countries and upwards of 2 500 scientists contribute to the ATLAS experiment.

3.2.3 Measurements at the ATLAS Detector

The ATLAS detector uses a right-handed set of coordinates for measuring positions. The detector itself is described by a Cartesian plane with the z-axis along the beam pipe. The x-axis points to the centre of the LHC ring and the y-axis points in the upwards direction.

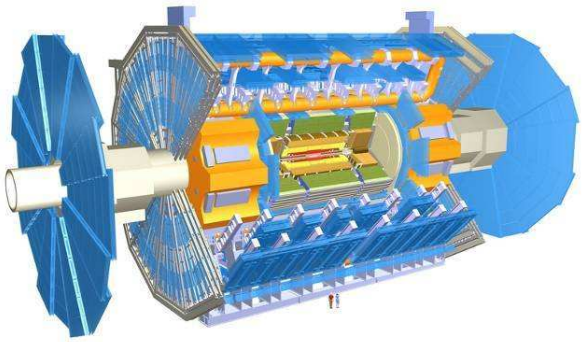

Figure 3.6: The ATLAS detector at CERN.

Since the particles in the collider are moving at relativistic speed, the detector is described by the pseudorapidity η and the azimuthal angel ϕ. The pseudorapidity is used to describe a spatial coordinate relative to the beam axis. This can be seen on the ATLAS detector in Fig. 3.7.

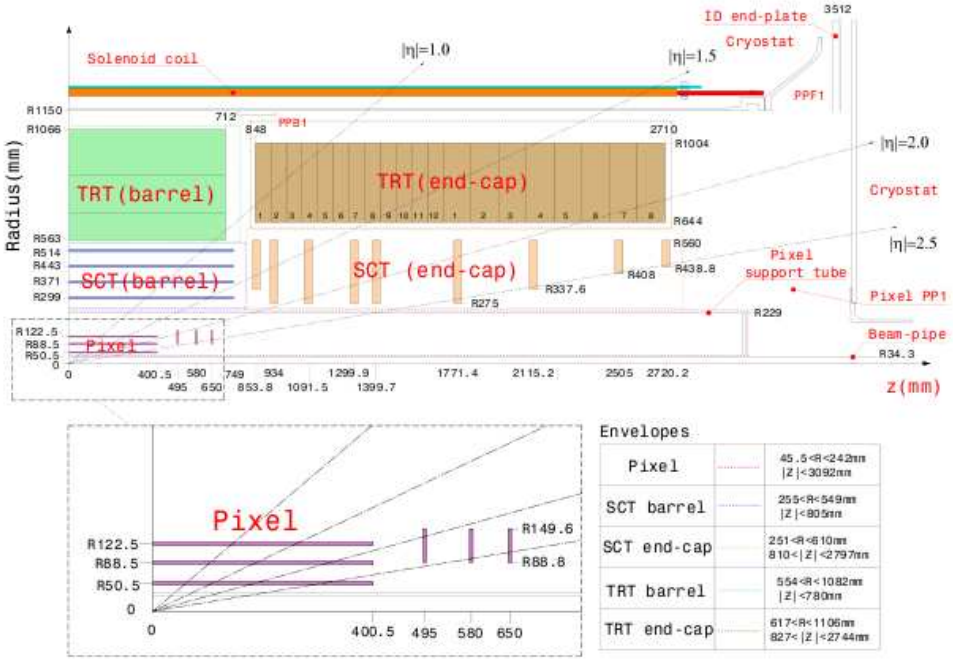

Figure 3.7: ATLAS detector with different angles of pseudorapidity η.

The pseudorapidity η is given by the formula

$$\eta = -ln\left[\tan\left(\frac{\theta}{2}\right)\right], \tag{3.1}$$

where θ is the angle between the beam axis and the direction of the particle.

Pseudorapidity is used in relativistic hadron collider physics due to the fact that the displacement in η is Lorentz invariant. The particle rate should be largest at large η and consequently the $\Delta\eta$ is very small. As one moves close to 90° from the beam pipe it can be seen that $\Delta\eta$ is very large. The particle rate per $\Delta\eta$ is constant.

Hadron colliders involve the interactions of quarks and gluons with unknown inital longitudinal momentum and energy. Therefore, transverse quantities of energy E_T and momentum p_T are used. Before the interaction the sum of all the transverse quantities is zero. After the interaction, the addition of all the vectors can be calculated to determine missing transverse energy (MET). From this, particles such as neutrinos or SUSY particles can be deduced without being seen directly.

3.2.4 Main Components of the ATLAS Detector

The inner detector [28] is situated close to the beam pipe. Its purpose is to allow precise position measurements and tracking. It is devided into three separate parts: the pixel detectors, the semiconductor tracker (SCT) and the transition radiation tracker (TRT). This can be seen in Fig. 3.8.

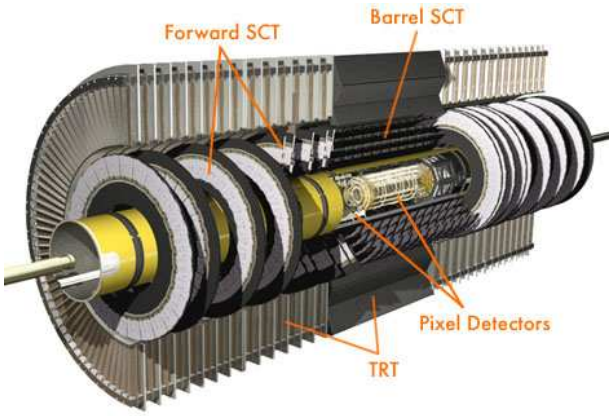

Figure 3.8: The inner detector of the ATLAS detector. It contains the pixel sensors, silicon strips and the TRT.

The pixel detectors are silicon semiconductor detectors which detect charged particles by the energy deposited in the depleted zone. The pixel detector has three cylindrical layers. Overall, it has a radial extension from the beam pipe between 45.5 mm to 242 mm. It covers an η range of up to 2.6. The silicon material itself is 250 μm thick. In total, the pixel detector has over 80 million readout channels.

The SCT is a silicon strip detector. Again, using silicon as a semiconductor, the strips cover a larger region than the pixel. The layers of strips are placed one on top of the other, with a 40 rad angle between verticle layers. This is done to reduce ghost hits which are created when a signal is detected on two strip detectors at the same time. The SCT has strips of 80 μm by 12.6 cm. The total SCT is comprised of four double layers and 6.2 million readout channels.

The two silicon sections of the inner detector play an important role in determining the particles' momenta. Using the 2 T solenoidal magnetic field, a particle is bent as it moves through the inner detector. Depending on the sagitta in the trajectory of the particle, the particle's momentum can be calculated. The solenoidal and toriodal windings which produce the magnetic field can be seen in Fig. 3.9.

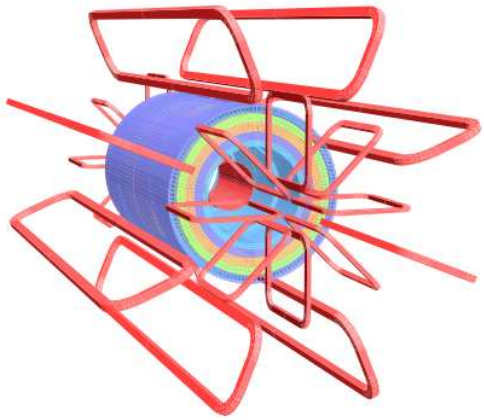

Figure 3.9: A view of the ATLAS magnets. The round barrel in the centre is the solenoidal magnet whereas the rings to the outside form the toroidal magnets.

For the ATLAS experiment, the resolution on momentum measurements using the inner detector and muon spectrometer is given by:

$$\frac{\Delta p_T}{p_T} = 0.04\% \cdot p_T \oplus 2\% \tag{3.2}$$

in GeV. These values are the result of the magnetic field and components of the detector. For a muon, the momentum can be measured in the muon spectrometer as well as in the inner detector. This is done by measuring the sagitta of a particle's trajectory as it traverses through the spectrometer. The sagitta measurement is shown in Fig. 3.10. The muon tubes and the measurements of the muons will be further discussed in a later section.

The TRT straw detectors are Xenon filed gas straws which are used to measure the transition radiation of particles. Transition radiation is created as the particle goes through the plastic radiation producer. Different types of particles produce a different number of transition radiation photons which are detected by the TRT. This will allow particle identification. This is especially of interest for identifying pion background on event by event basis, as opposed to over the collective whole. The straw tubes each have a diameter of 4 mm and take up a 7 m long section

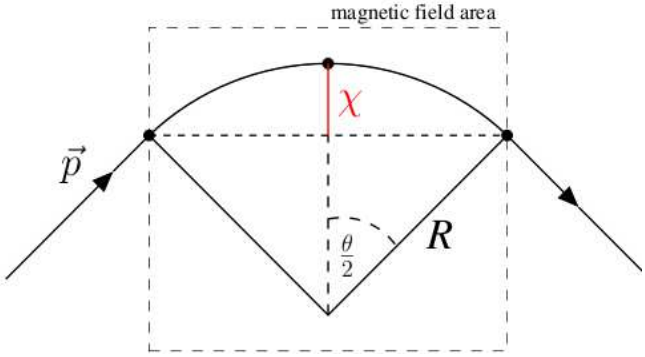

Figure 3.10: The trajectory of a particle due to a magnetic field. The particle's trajectroy is bent, creating the sagitta, χ, which can measure the momentum of a particle due to its size.

of the detector, starting from 0.6 m to 1.1 m. The barrel section of the TRT, along with the inner detector and the calorimeter can be seen in Fig. 3.11.

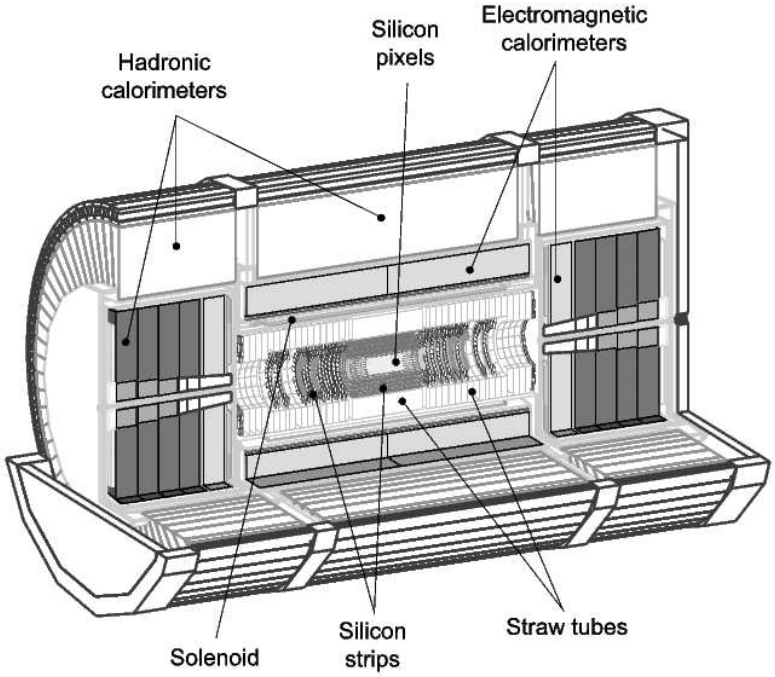

Figure 3.11: The inner detector and both the electromagnetic and hadronic calorimeter.

There are a total of about 400 000 straws with a diameter of 4 mm and a 30 μm gold plated tungsten wire in the centre of each tube. The straw is filled with a 70% Xenon, 27% CO_2, and 3% O_2 solution. The Xenon is used to detect the transition radiation photons created by a radiator, which is much like a plastic material, in between the straws.

Calorimeters [29] are used to determine the energy deposited by single particles, such as electrons, or by a jet of particles. It collects the position and amount of energy per event. The

calorimeter is split into two components, the electromagnetic and hadronic calorimeters.

The electromagnetic or liquid Argon calorimeter [30] is found directly outside the inner detector when going outward from the beam pipe. The liquid Argon calorimeter is used to absorb the energy from the electromagnetic particles. It is an accordion shaped lead absorber device filled with liquid Argon, nominal at temperatures of approximately 87 K. The length of the barrel section of the liquid Argon calorimeter is over 24 radiation lengths, denoted as X_0, which is the length for a particle to lose 7/9 of its energy, to allow for the full decay of the particle into the calorimeter. The end cap succeeds 26 radiation lengths. The energy resolution on the electromagnetic calorimeter is

$$\frac{\Delta E}{E} = \frac{11.5\%}{\sqrt{E}} \oplus 0.5\% \tag{3.3}$$

in GeV.

Electromagnetically interacting particles (e.g. photons and electrons) create a shower of particles inside the calorimeter. The lead walls cause a cascade of particle creation inside the calorimeter. The electrons emit photons which then create an electron - positron pair. This interaction can be parametrized be the radiation length. This process continues until new photons or pair productions cannot occur. All of this energy and particles are absorbed in the calorimeter and the energy is recorded. This shower effect can be seen in Fig. 3.12.

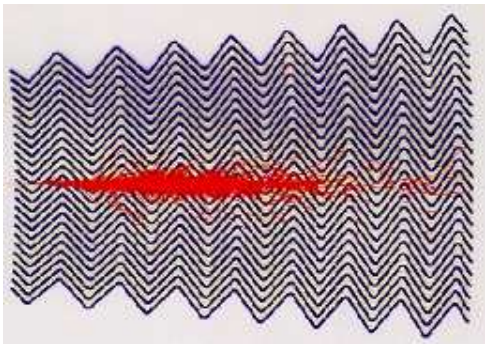

Figure 3.12: A particle shower in the accordian shaped electromagnetic calorimeter.

The hadronic calorimeter at ATLAS is build of tile scintillators which measure light in wavelength shifting fibers [31]. It uses iron absorber plates and scintillating tiles as the active medium. As the hadrons enter the calorimeter, they begin their showering in the electromagnetic calorimeter. They deposit the rest of their energy into the hadronic calorimeter by creating scintillating light detectable by the tile calorimeter. The set-up of the hadronic tile can be seen in Fig. 3.13.

An interesting feature of the tiles in the calorimeter is their radial placement. This is done to allow the hermicity of the calorimeter which still allows the routing of read-out fibres and cables, which would not be possible if the tiles were not placed in the same orientation as the incoming particles. This orientation is shown in Fig 3.13. The hadrons' directions are parallel to the plane of the tile.

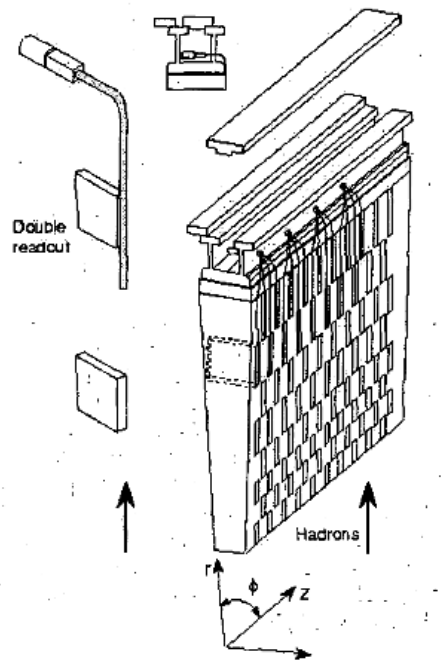

Figure 3.13: Schematic drawing of the tile calorimeter. The hadrons will come from below, parallel to the placement of the calorimeter.

The energy resolution of the tile calorimeters in GeV is:

$$\frac{\sigma}{E} = \frac{42\%}{\sqrt{E}} \oplus 1.8\% \oplus \frac{1.8\%}{E}. \tag{3.4}$$

The muon detectors [32] are the largest of the ATLAS subdetectors, and form the exterior part of the experiment. The different sections of the muon spectrometer are shown in Fig. 3.14. There are a total of 370 000 muon tubes on the ATLAS detector, measuring 1.5 cm in radius, with a 30 μm radius aluminium wire in the centre.

The muon spectrometer is used to measure muon properties: the momentum, the charge, and the position. The spectrometer sits inside a superconducting toroidal magnet system, which bends the particle as it traverses through the muon spectrometer. As opposed to the inner detector where bent trajectories are due to the solenoidal field, the toroidal field bends the particles in the muon spectrometer.

Since the muon is a minimum ionizing particle at about 1 GeV it is the only visible particle to escape the inner detector and calorimeters. Therefore a muon system on the exterior of the detector is used to detect it and distinguish it from other particles. The spectrometer is also set to trigger as a muon traverses through the spectrometer with trigger chambers: Thin Gap Chambers (TGCs) and Resistive Plate Chambers (RPCs).

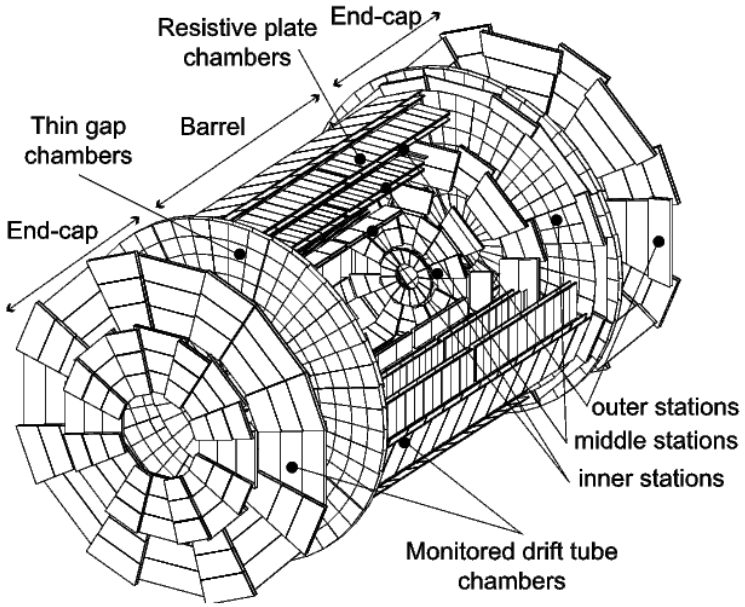

Figure 3.14: View of the different stations of the muon spectrometer forming the exterior of the ATLAS detector. The three sections are the inner, middle and outer stations.

The barrel region contains three RPCs in order to trigger upon the detection of a muon. They are also used to add coordinates for position measurements. In the end cap regions, three layers of TGCs are used for triggering.

The muon chambers are set to measure with a resolution of up to 3 % for 10-200 GeV and 10 % for 1 TeV muons. For 1 TeV muons, a 10 % resolution corresponds to a sagitta of about 500 μm. The measurement of the sagitta has to be done with a resolution of 50 μm.

To measure the position of the muons, the spectrometer contains three stations or layers: the inner, middle, and outer stations. These stations are found on the barrel and end cap regions. The three stations in the barrel are concentric cylinders with a radius of 5 m, 7.5 m and 10 m. Together, they cover an η range of up to 1.

With the position of three stations, the muon momentum is able to be measured from the sagitta created due to the toroidal magnetic field. In the central region, η up to 1, the muon momentum is measured in the Monitored Drift Tube Chambers (MDTs). In the end cap region, extra chambers are used to measure the momentum and trajectories of muons.

For the η regions between 1.0 and 2.7, the four concentric end cap layers of 7 m, 10 m, 14 m, and 21-23 m from the centre of the detector are used for measurements. In these regions both MDTs and Cathode Strip Chambers (CSCs) are used. The CSCs are found in the inner station close to the beam pipe due to the high level of radiation.

For the triggering of muons, the RPCs have 544 chambers with 359 000 readout channels. They cover an area of 3 650 m^2. The TGCs have 3 588 chambers with 318 000 readout channels,

covering an area of 2 900 m^2. For the momentum measurements, the MDTs have 1 088 chambers, with 339 000 readout channels and an area of 5 500 m^2. The smallest chambers are the CSCs with 32 chambers, 30 700 readout channels, covering only an area of 27 m^2. The muon chambers can also be seen in Fig. 3.15 and 3.16.

3.2.5 Muon Ionizations inside the MDT

Muons create a signal in the MDT through ionization of the Gas. The tube is composed of 93 % Ar and 7 % CO_2. As the muon passes through the gas, it creates ions and electrons due to ionization. These electrons drift towards the Al wire according to the electric field inside the tube, the ions drift towards the wall of the tube. It is in this process where a signal is created due to the addition of electric charge at the wire and the buildup of ions along the exterior of the tube.

Inside the tube, "delta-electrons" are created by ionized electrons which collide with atoms. These "delta-electrons" are the small fraction which have large energies compared to the ionizing potential. This causes errors in the signal and possibly the creation of secondary tracks. The ionized electrons also diffuse as they drift towards the wire. This is all taken into account so that the arrival of the signal will allow the position of the initial muon track to be reconstructed.

The muon chambers also require multiple chambers to accurately describe the position of the muon. Since the signal is only based on the arrival of the charge, a single tube can only locate the distance from the wire to which the muon passed. With the addition of multiple tubes, the location of the track can be determined.

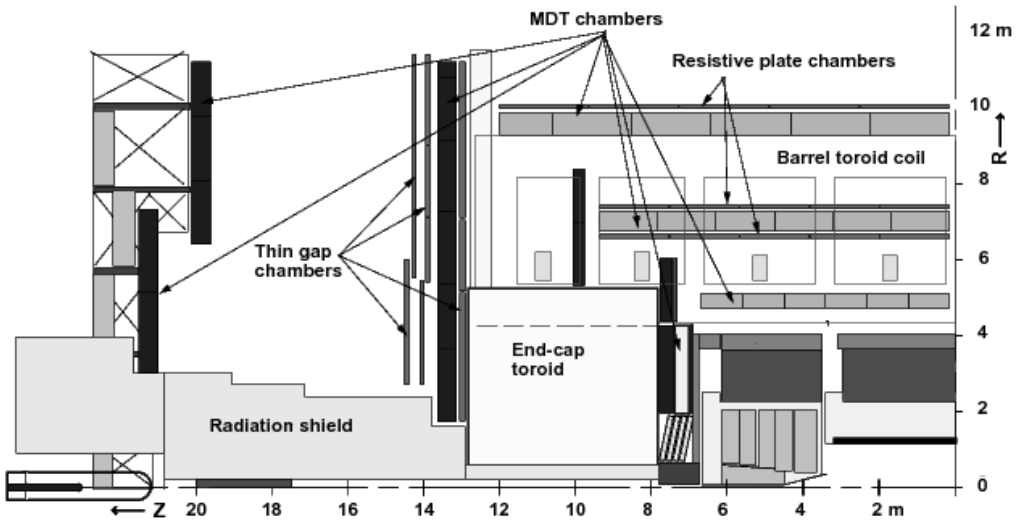

Figure 3.15: One Quadrant of the Muon Spectrometer of ATLAS.

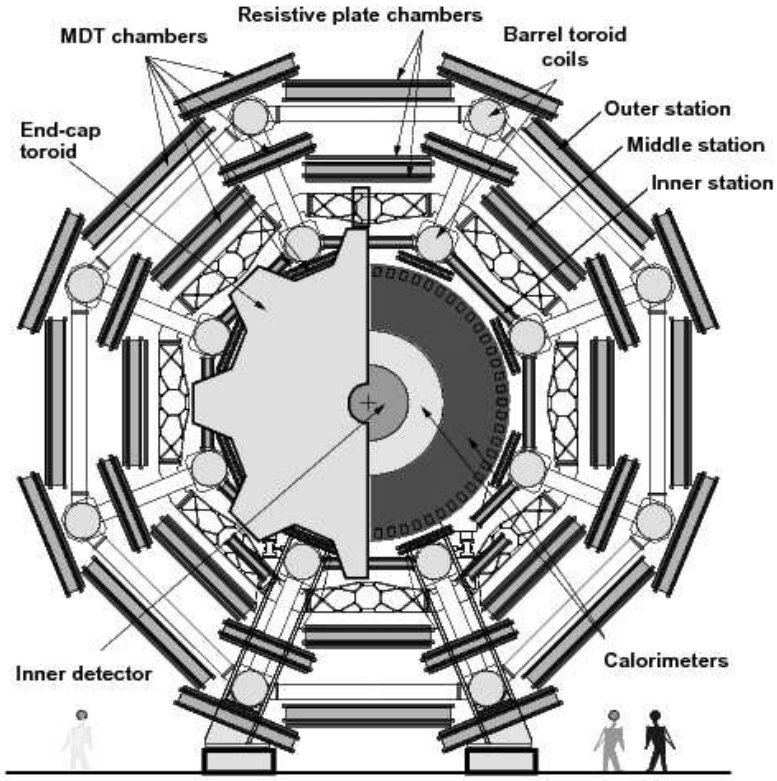

Figure 3.16: Side View of the Muon Spectrometer of the ATLAS experiment.

4 Germanium-76 Detector Analysis

4.1 Experimental Project Description

This project attempts to study the properties of a p-type Germanium detector with respect to the noise due to ultraviolet light and infrared light. This is important in the context of the GERDA experiment since in Phase I of the experiment, the Ge detector will be submerged in liquid Argon. Argon is a scintillator which also radiates in the UV-range. It thus needs to be tested whether this UV-light significantly increases the noise level of the Ge detector.

This section is part of an internal note prepared also for the GERDA Collaboration at the Max Planck Institute for Physics in Munich, Germany.

4.2 Experimental Setup

It is important to study the ^{76}Ge detector in order to understand its properties under certain situations. The ^{76}Ge detector is a semiconductor which is sensitive to energy deposition due to photons and charged particles. It is necessary to distinguish between the signal and background, to minimize the background.

It is uncertain whether the setup of the GERDA experiment may be inadequate in suppressing background in the form of cosmic radiation. Since liquid Argon is a better shield against this background and it is only 10 K higher in temperature than liquid Nitrogen, it is a suitable canditate for the liquid tank which houses the detector. Even though liquid Argon seems to be a more suitable replacement over liquid Nitrogen, it can produce scintillation light. It is still uncertain whether this light will create photons which could cause noise in the detector. Therefore this process needs to be tested in order to determine whether or not liquid Argon is a suitable candidate.

For this experiment, four different types of Light Emitting Diodes, or LEDs, were placed so that the light was able to shine down into the glass dewar. These LEDs simulated the scintillation light from liquid Argon. Inside this dewar, the sixfold segmented germanium detector was submerged in liquid Argon. This setup will show the effect of different fluxes of photons at different wavelengths onto the detector.

First off, all the properties of the diodes were measured and analyzed. The four wavelengths of the diode are 360 nm, 380 nm, 400 nm, and 1100 nm. This allows the examination of a range in the UV spectrum, close to that of the scintillation wavelength from liquid Argon at around 120 nm. Studies were also done in the IR spectrum. Once the properties of the diodes were determined at 87 K, the resistance of the diodes was calculated as a function of temperature. In this part, to measure the temperature in the dewar at a specific height, the resistance of a piece

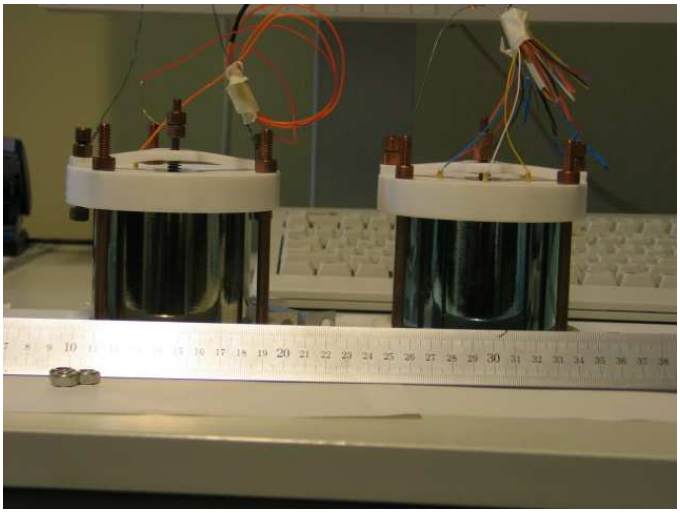

Figure 4.1: Two six fold segmented ^{76}Ge detectors used at the Max Planck Institute for Physics in Munich.

of ^{100}Pt was measured. Since the resistance of ^{100}Pt can be easily converted into temperature using a well known formula, the temperature vs. resistance of the diode could be plotted.

The detector was then used to measure the leakage current due to the diodes. This leakage current was measured by placing the LED on the top of the dewar, shining the light inside. The current through the diode was then raised and the change in leakage current was noted. The leakage current was measured using a Keithley picoammeter. Afterwards, 30 minute measurements were made of the Co-60 spectrum and the resolution of the Full Width at Half Maximum (FWHM) was noted. The radioactive ^{60}Co source was attached to the outside of the metal dewar containing the ^{76}Ge detector inside. To make note, ^{60}Co is a beta-decay with a half-life of 5.24 years. ^{60}Co decays into ^{60}Ni with the release of an electron and an anti-neutrino. It releases two gamma-rays at 1.17 MeV and 1.33 MeV, which are then measured for resolution on the spectrum. The decay information on the decay of ^{60}Co is taken from [33]. To see the change in resolution due to the UV light, the voltage and subsequent current were increased on the LED diodes and the resolution of the peaks were again measured for different amounts of current through the diode. The energy spectrum was analyzed for the core of the detector; the complete energy deposited in all six segments.

4.2.1 Setup of the Test Stand

The test stand set-up at the Max Planck Institute in Munich, Germany, is shown in Fig. 4.2. The test stand is a solid metal cylinder which accomodates a dewar. It contains glass walls on the inside. The six-fold segmented detector is hung from the top of the test stand and submerged into the liquid Argon, which fills the dewar.

On the top of the test stand there is a hole, which allows the LED to shine on the detector. Original designs had the light placed directly into the liquid Argon, however this proved not to be useful since it was undetermined whether the LED was working inside the liquid argon.

Figure 4.2: Test stand used for this experimental analysis. It is a small version of the GERDA set-up at LNGS in Italy. The detector is suspended into the liquid Argon dewar.

Therefore a design was made so that the light could sit at the top surface of the liquid argon, shining down onto the detector. This design allowed for the LEDs to not be submerged with liquid Argon, yet still shine onto the detector, simulating scintillation light. The LEDs are controlled by external sources in order to calculate their current.

The germanium detector was attached to a high voltage supply which was set to 2 500 V. The leakage current was measured by a pre-amplifier placed on the top of the detector. It measured the leakage current from the six different sections of the detector separately. Afterwards they were added together to calculate the total leakage current for analysis.

4.3 LED Light Properties and Calibration

4.3.1 LED Light Properties at Room Temperature and in Liquid Argon

The LED wavelengths which are used for the analysis are 360 nm, 380 nm, 400 nm and 1100 nm. The 360 nm diode was also used at liquid Argon temperatures of approximately 87 K but did not work as expected. Therefore, its IV curve was not plotted at 87 K. These light calibrations are done inside the liquid Argon to check if they could also be directly submerged

along with the detector. However, the LEDs were left outside the liquid Argon filled dewar for the experimental procedure due to the results plotted in Fig. 4.3.

To fully understand the exact manner in which the diodes would affect the detector, the properties of the diodes themselves had to be measured. Firstly, a current versus voltage (IV) plot was made of all the diodes at 300 K and 87 K. The three which worked at 87 K showed a shift of the curve when dipped into the liquid Argon. This translation correlates to the change in semiconductor properties of the diodes. As can be seen in the figures below, at 87 K the current through the diode does not grow until higher voltages are reached across the diode. Also note, all current is in the positive direction through the diode.

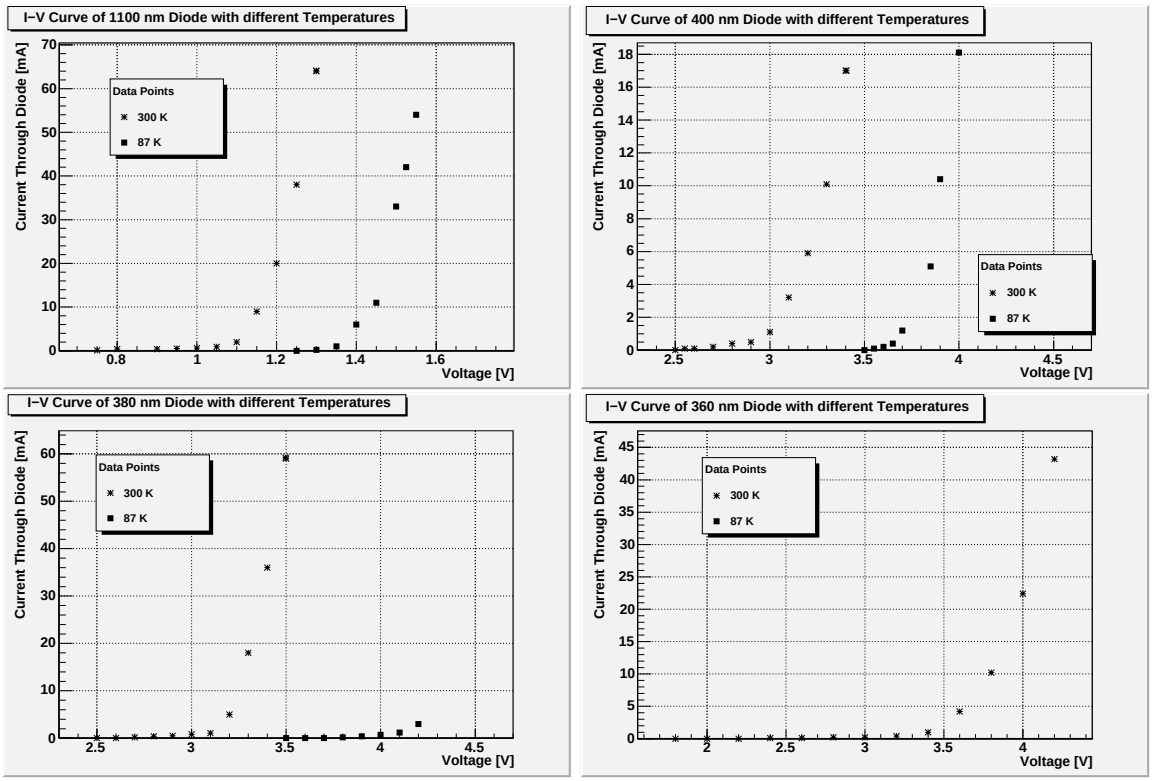

Figure 4.3: IV curves for the four different diodes used in the experiment. All show a shift in the positive curve. The 380 nm UV diode at 87 K had to be stopped at approximately 4.2 V because the 220 Ω resistor became extremely hot. The 360 nm UV diode did not perform properly in liquid Argon, so only its 300 K curve is plotted.

All curves exhibit the semiconductor properties associated to current flow in the positive direction, and the 1100 nm, 400 nm, and 380 nm all worked in the liquid Argon at 87 K. The same properties can be seen at that temperature as well, with only a shift in the curve. This is due to the fact that at lower temperatures, the energy gap of the semiconductor gets larger. This means that photons released are less likely, resulting in higher resistivity and lower current running throught the diode at the same voltage. However, this also relates to another property of the diodes which could not be tested. Since the energy gap rises, the photons which are released are of higher energy and lower wavelength. This is not a problem for this experiment since lower in the UV range is a closer wavelength to Argon. When Argon scintillates, it produces

photons with 120 nm wavelength, far smaller than the lowest used in this experiment of 360 nm. Therefore, if the wavelength of the diodes drops as speculated, it only helps better recreate the effects of the lower UV range. Overall though, the diode does change properties when put at 87 K, as seen in the preceeding graphs, the current drops over the same voltages due to an increase in the energy band gap of the semiconductor inside the diode.

4.3.2 LED Temperature Dependence Properties

LED lights are semiconductor diodes, as a result, they are temperature sensitive. Therefore it is important to understand the properties of the diodes when they are placed inside the dewar. For this measurement, only the 380 nm diode was used.

The 380 nm diode was lowered into the dewar, and its resistance was measured at every centimeter down into the dewar until it reached the Liquid Argon. The same was done to measure the temperature, at every centimeter, the resistance of the ^{100}Pt slab was measured.

The equation used to convert the resistance of the ^{100}Pt into temperature is:

$$R_t = R_0 \cdot [1 + (A \cdot t) + (B \cdot t) + [C \cdot (t - 100)] \cdot t] \tag{4.1}$$

Where:

$$\begin{aligned} A &= 3.9083 \cdot 10^{3} \\ B &= -5.775 \cdot 10^{-7} \\ C &= \begin{cases} -4.183 \cdot 10^{-12}, & \mathrm{T} < 270K \\ 0, & \mathrm{T} > 270K \end{cases} \\ R_0 &= 100\Omega \end{aligned}$$

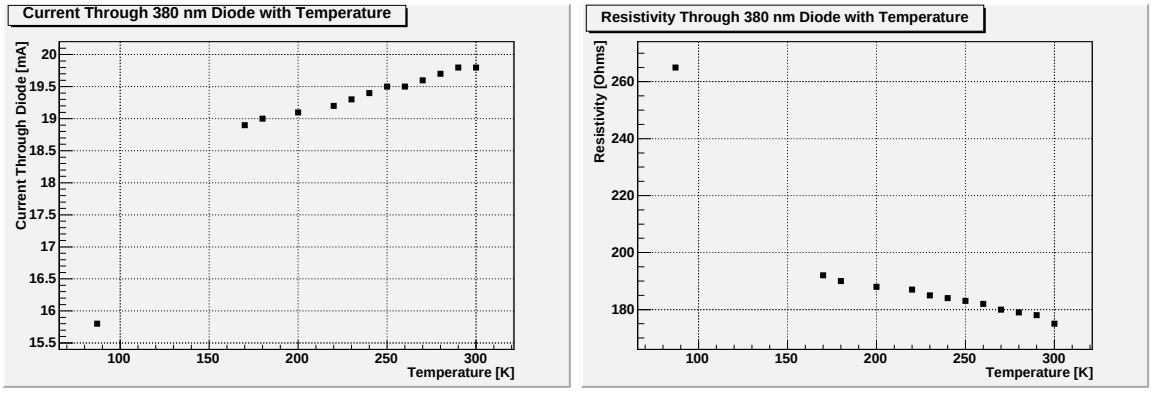

Figure 4.4: The graph on the left shows the relationship between current and temperature while the second graph shows the relationship between resistance of the diode and temperature. The change in the energy band gap of the semiconductor causes a retarded current flow and a higher resistance of the diode.

The two graphs in Fig. 4.4 show that the diode properties are dependent on the temperature. This is expected because the diode is a semiconductor. The 380 nm diode becomes more resistive at lower temperatures. The plot is almost linear as the temperature decreases, but once it touches the liquid Argon at 87 K, the resistivity rises significantly. Also, once the diode is inside the liquid nitrogen, it stays at the same resistivity for a prolonged period of time. Even if the diode is continued to be lowered after entering the liquid nitrogen, neither time nor depth have an effect on its resistivity. This means that the 380 nm UV diode can be used to measure temperature and/or level of liquid Nitrogen or Argon in a dewar either by measuring its resistivity or by its current. When the diode enters the Liquid Argon, the resistivity jumps out of the linear plot and rises to a higher value; this can be seen in the graph in Fig. 4.4. This is expected and can also be seen from the IV curves in the previous section. At liquid Argon temperatures, the IV curve is shifted to the right, meaning a higher resistivity of the diode due to an increase in the energy band gap as described earlier. The diode's linear resistance vs. temperature graph is shifted once it touches the liquid Argon and the resistance rises on the diode due to lower currents over the same voltages while it is not submerged at 87 K. The low temperature causes the energy band gap to rise, resulting in a measurably smaller amount of current flowing through the diode effectively creating an impedence of current flow and a higher resistance. This explanation is continued in the discussion along with several other possible reasons for the phenomena noticed with the diode.

4.4 Analysis of Ge-76 Detector's Reaction to Photons Produced by LEDs

4.4.1 Leakage Current produced by LEDs

In this section, the leakage current through the detector produced by the diodes is investigated. Each diode was placed on the top of the detector and the photons were shot into the detector. Since it is known that the current through the diode is proportional to the photon flux, changing the current has the same proportionality to changing the amount of photons which are being released by the diode. Knowing this, it is important to understand which currents result in the same photon flux from the different diodes. With this, whether or not the detector reacts similarly to different wavelengths of light can also be checked.

At first, the IR diode of 1100 nm was tested to make sure the detector was working properly. The ^{76}Ge detector is very much affected by IR light, and so in this measurement, a high leakage current is expected. In this case, there also was a shield protecting the detector from the IR light, but has small holes in which the IR light that is placed on the top of the dewar, pointing inward, can still reach the detector. The leakage current was measured at different intervals of applied current into the diode.

In Fig. 4.5, it can be seen is that the detector is effected by IR light as expected. As the current through the diode is increased linearly, also meaning the photons released by the diode increase linearly, the leakage grows linearly proportional as a direct result of this. Even with a shield protecting the detector, there is still a profound effect as a result of such IR light. Therefore, the detector must be shielded against any such IR light as to not cause a rise in the leakage current, and subsequently, a worse resolution when using the ^{76}Ge detector. This also proves that the detector is working properly since there were problems originally with the leakage

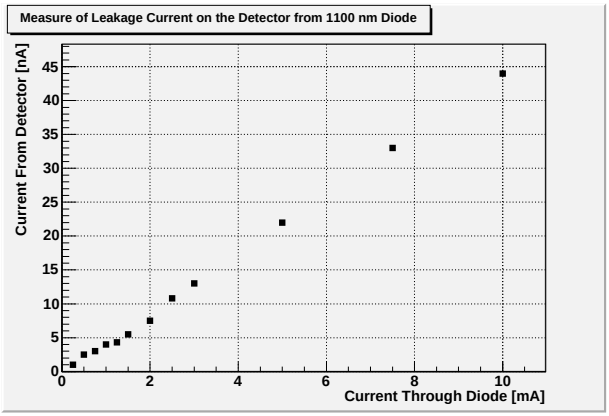

Figure 4.5: Leakage current over the whole detector as a result of infrared light at 1100 nm being put on it. The detector reacts linearly to the light as expected. As the number of photons hitting the detector increases linearly, the leakage current on the detector also increases linearly.

current values obtained at the start of the experiment. With this known, the measurements of the UV light can be now tested knowing the detector is functioning as it should.

The first UV diode that was tested was the 400 nm diode. The leakage current was checked for different values of current through the diode.

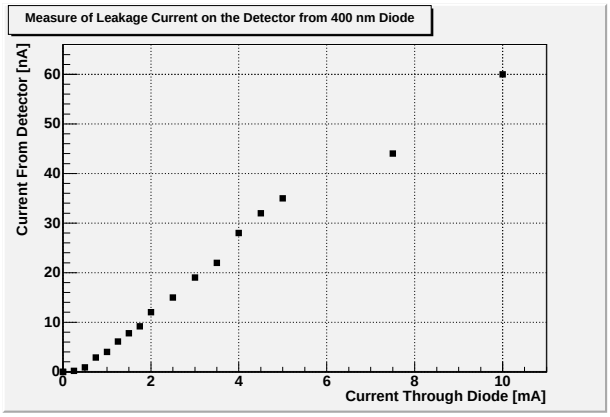

Figure 4.6: Leakage current from all segments of the ^{76}Ge detector when different amounts of 400 nm wavelengths are seen by the detector. The results show the leakage current is linearly proportional to the amount of photons released by the diode at 400 nm.

Within the GERDA Collaboration, there is interest in submerging the crystals in liquid Argon instead of liquid Nitrogen. Due to the extreme sensitivity, liquid Argon would produce a more stable liquid to submerge the crystals in, while keeping the detectors cold. As can be seen, the detector reacts linearly with the rise in current through the diode. This is expected and means that the leakage current is directly proportional to the photons hitting the detector, and can be deemed the reason for the increase in the leakage current on the detector. As the amount of 400 nm UV photons hit the detector increases, the detector has more and more leakage current. Eventually, at high enough photon fluxes on the detector, the leakage current is extremely high

and can cause severe problems when making measurements using the ^{76}Ge detector. However, 400 nm is still in the visible range and therefore the detector should detect these photons. Therefore further analysis into the lower wavelengths will give us more information.

The second diode measured was the 380 nm diode. The same procedure is followed for the 400 nm diode as for the 380 nm diode. The studies of its leakage current follow.

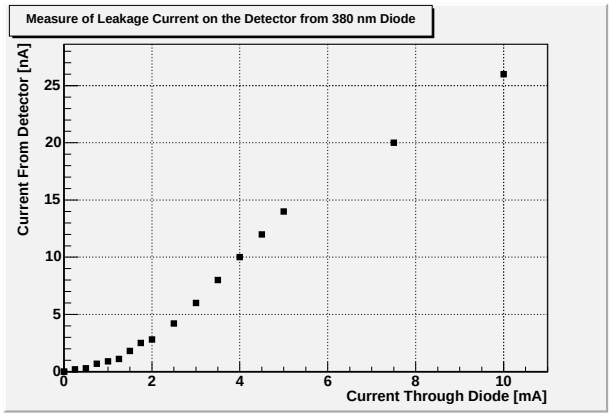

Figure 4.7: Leakage current from all segments of the ^{76}Ge detector when different amounts of 380 nm light are hitting the detector. Again, the leakage current grows significantly higher as the number of photons are increased.

The 380 nm wavelength diode's effect is again almost linearly proportional in terms of the leakage current of the detector and the input current through the diode. This is as expected and shows that the detector is responsive to the photon flux produced by the 380 nm UV light range. As a result, it can be deemed that the detector is significantly affected by the 380 nm light, again causing concern with the use of liquid Argon. Finally, the 360 nm diode was measured.

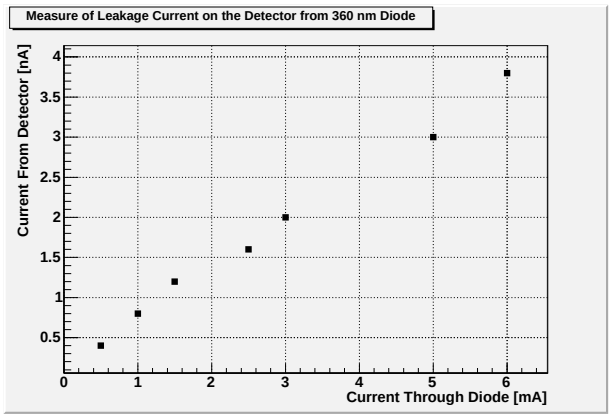

Figure 4.8: Leakage current from all segments of the ^{76}Ge detector when different amounts of 360 nm light are hitting the detector. Again, the leakage current grows significantly higher as the number of photons are increased.

Again, the detector has a similar translation to the photon flux of the diodes. However, when looking at the graphs more closely, the amount of leakage current is not the same for each wavelength of light. This can either be because of two reasons, the first is that the detector sees less UV light as one goes to smaller wavelengths. The second is that the release of photons by the diodes is different. Therefore, to test how much output photon flux each diode was producing, a phototransistor was used. The voltage over the phototransistor was measured for each diode. For a voltage change of 0.25 V on the phototransistor, the current through the different diodes was measured and placed in the following table.

Current on Diode Corresponding to 0.25 V Change on Phototransistor

Wavelength of Diode	*Current Through Diode*
400 nm	1.05 mA
380 nm	2.3 mA
360 nm	10.00 mA

Table 4.1: This table shows the amount of current running through the different diodes which result in the same change on the phototransistor. In other words, it is to find the currents through each diode to determine which produce the same number of photons. The 400 nm diode produces the most photons, approximately 2 times as much as the 380 nm diode and approximately 10 times as much as the 360 nm diode.

When looking at this table, it can be seen that the photon flux is very different for each diode. The 400 nm diode is 10 times greater in photon output than the 360 nm diode is. Therefore, when looking at the 360 nm diode in Fig. 4.8, for 10.0 mA of current, the leakage current is 7.9 nA. Then when looking at Fig. 4.7, the leakage current at 2.3 mA through the diode is approximately 4.0 nA. When corresponding to the 400 nm diode in Fig 4.6, the leakage current at 1.0 mA through the diode is again about 4.0 nA. This means that the leakage current at the same output of photon flux is pretty similar. Therefore, the detector reacts similar to all three UV diodes, even though they have different wavelengths. This is as expected because the wavelength change between diodes is very small, though relevant.

4.4.2 Measuring the Photon Flux Hitting the Detector

Now that it is known the detector reacts similarly to the three UV diodes at the same photon flux, the number of photons which hit the detector must be known to be able to compare with their effects on the leakage current. Since the number of photons which are produced by scintillation of Argon can be estimated, a determination as to how they will effect the detector can be made by comparing it to the effects seen in this experiment. Therefore it is important to know what magnitude of photons are being seen here.

The leakage current through the detector is given by the equation

$$I_{leakage} = \frac{N_e \cdot e}{1\ \mathrm{s}} \tag{4.2}$$

where $I_{leakage}$ is the current through the detector, N_e is the number of electrons, and e is the elementary charge. Also, the number of electrons can be used to calculate the number of photons

from

$$N_\gamma = \frac{3 \text{ eV} \cdot N_e}{E_\gamma} \tag{4.3}$$

where N_γ is the number of photons released by the diode and E_γ is the energy of one photon. In this case, it can be deemed that the energy of one photon be approximately 10 eV for the UV range used. The 3 eV is the energy per electron-hole pair in the Germanium semiconductor at 87 K [34].

Putting the two equations together to calculate the number of photons per second gives:

$$N_\gamma/\text{s} = \frac{3 \text{ eV} \cdot I_{leakage}}{E_\gamma \cdot e}. \tag{4.4}$$

Now that the method in which the number of photons released from the diode which deposited energy on the detector can be calculated, the number of photons which scintillation of Argon produces must be known. Through previous known calculations, the number of photons produced by the scintillation light of Argon is approximately 40 000 photons/second.

If the number of photons which hit the detector per second is of the order of 40 000, the calculations yield a leakage current of the detector to be on the order of $2 \cdot 10^{-14} A$ or $2 \cdot 10^{-5} nA$. This means that when the Argon scintillizes and produces UV photons of the order of 120 nm, the leakage current of the detector is extremely small. Therefore, in order to mimic such a bombarding of photons on the detector which would increase the leakage current by $2 \cdot 10^{-5} nA$, the UV diodes must have a small current running through them. If the graphs in the previous section are analyzed, it can be seen that even a small current running through these diodes will produce a significant number of photons which reach the detector. With our set-up, using the 380 nm UV diode at 0.25 mA, the number of photons which reach the detector is approximately $3.75 \cdot 10^8$ photons/second. This number is significantly higher than the number of photons when Argon scintillates. As a result, to really mimic the effects of scintillation, the diode must have a very small current running through it, approximately ≤ 0.1 mA. This is substantially small and if checked, causes no noticable change in the leakage current in this experiment. However, the leakage current of this Ge-detector was significantly high to begin with and therefore the precise accuracy of this claim is not very good. This means that the effects of these 40 000 photons, if any, should be almost unnoticable on the leakage current in the nanoampéres range.

Therefore, in the next section, the resolution of a ^{60}Co spectrum is analyzed and taken into account at different intervals of current running through the diode. This is to see the direct effect on the resolution, as a result of UV light hitting the detector and to see if the effects of 40 000 photons/second are significant enough to cause a change in resolution of the ^{60}Co spectrum.

4.5 Resolution of ^{60}Co Spectra when UV Light is put into Dewar

In this final section of the experiment, the direct effects of UV light were tested against the resolution of the 1.33 MeV peak of the ^{60}Co spectrum. The purpose of this is to determine if the UV light effects the resolution through the raise of leakage current, and if it does, determine if it is significant enough for concern.

To see such effects, the same setup as for the leakage current measuurements was used. Thirty minute spectrum measurements were made at different intervals of current on the diode. The first UV diode that was used was the 400 nm diode. This diode is the most powerful and therefore the ^{60}Co spectrum was analyzed while the diode had a current below 10 nA. Fig. 4.9 shows the effect of the increase in current through the 400 nm diode.

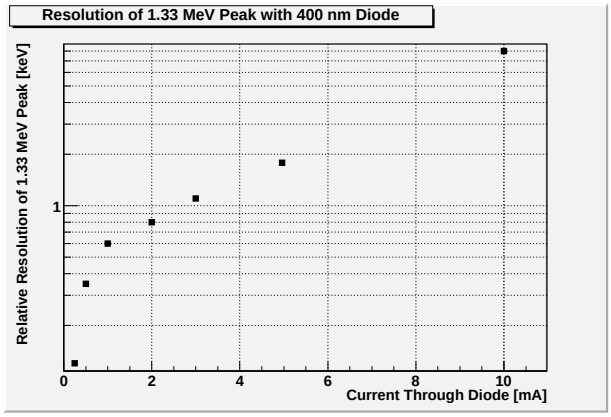

Figure 4.9: This shows the resolution change of the 1.33 MeV peak of the ^{60}Co spectrum as more and more photons are applied onto the detector using a 400 nm diode. As more photons hit the detector, the resolution worsens, making it harder to take good measurements due to the increase in 400 nm photons blinding the detector.

As can be seen, the current through the diode causes the resolution of the detector to become worse. This directly implies that the UV photons at 400 nm have an effect on the resolution of the detector. However, this is expected, 400 nm is not very far into the UV spectrum and therefore the detector should detect this value of wavelength. To see the effects on the total spectrum, several of the thirty minute spectra are in the next figure.

It can be seen by the spectra that the maximum number of counts on the two peaks at 1.17 MeV and 1.33 MeV become less as the current on the diode is increased. This is due to the blinding effect of the photons on the detector and also relates to the rise in noise energy which can be seen at the lower end of the spectrum. The peak at the low end of the spectrum continually increases as more photons at 400 nm wavelength are hitting the detector. The detector is being blinded by the deposited energy of these photons and cannot attain a good resolution of the peaks.

To test further into UV range, the 380 nm was tested. Its results were similar to the 400 nm diode.

Again, the signal is distorted with noise from the bombardment of UV light onto the detector. In Fig. 4.12, the change in resolution is again the same shape as the change in leakage current as in Fig. 4.10. This is because the rise in leakage current due to the increased amount of photons hitting the detector. This, in turn causes the resolution to become worse on the detector. What can be seen in the following figure, is the effects of the 380 nm on the detector when different amounts of photons are sent onto it.

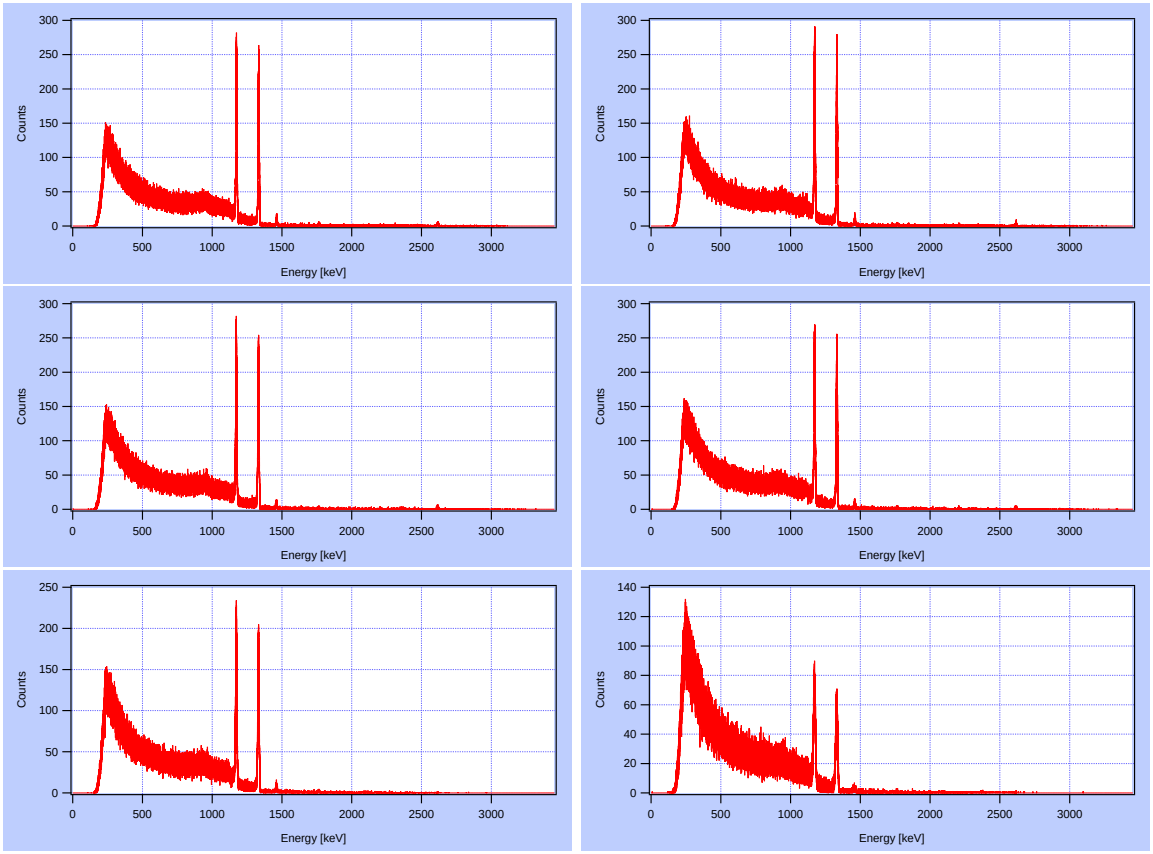

Figure 4.10: ^{60}Co Spectrum starting with current through the 400 nm diode at 0.0 mA (top left), then 0.5 mA (top right), 1.0 mA (middle left), 2.0 mA (middle right), 5.0 mA (bottom left), and finally 10.0 mA (bottom right). With the increase of current through the diode, and accordingly, the increase of the photon flux, the resolution on the ^{76}Ge detector gets worse.

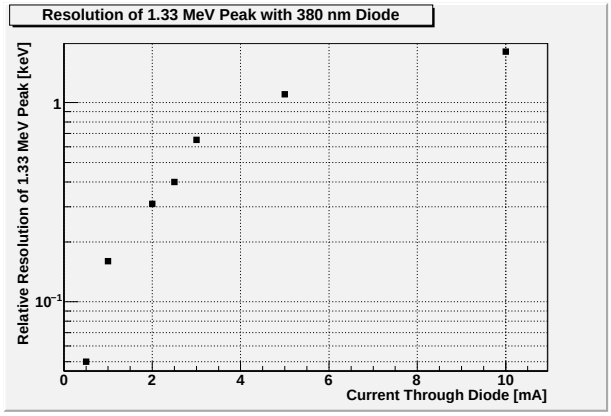

Figure 4.11: This shows the resolution change of the 1.33 MeV peak of the ^{60}Co spectrum as more and more photons are applied onto the detector using a 380 nm diode. Again, the effects of the 380 nm diode are similar to those of the 400 nm diode, as more photons are released, the worse the resolution becomes.

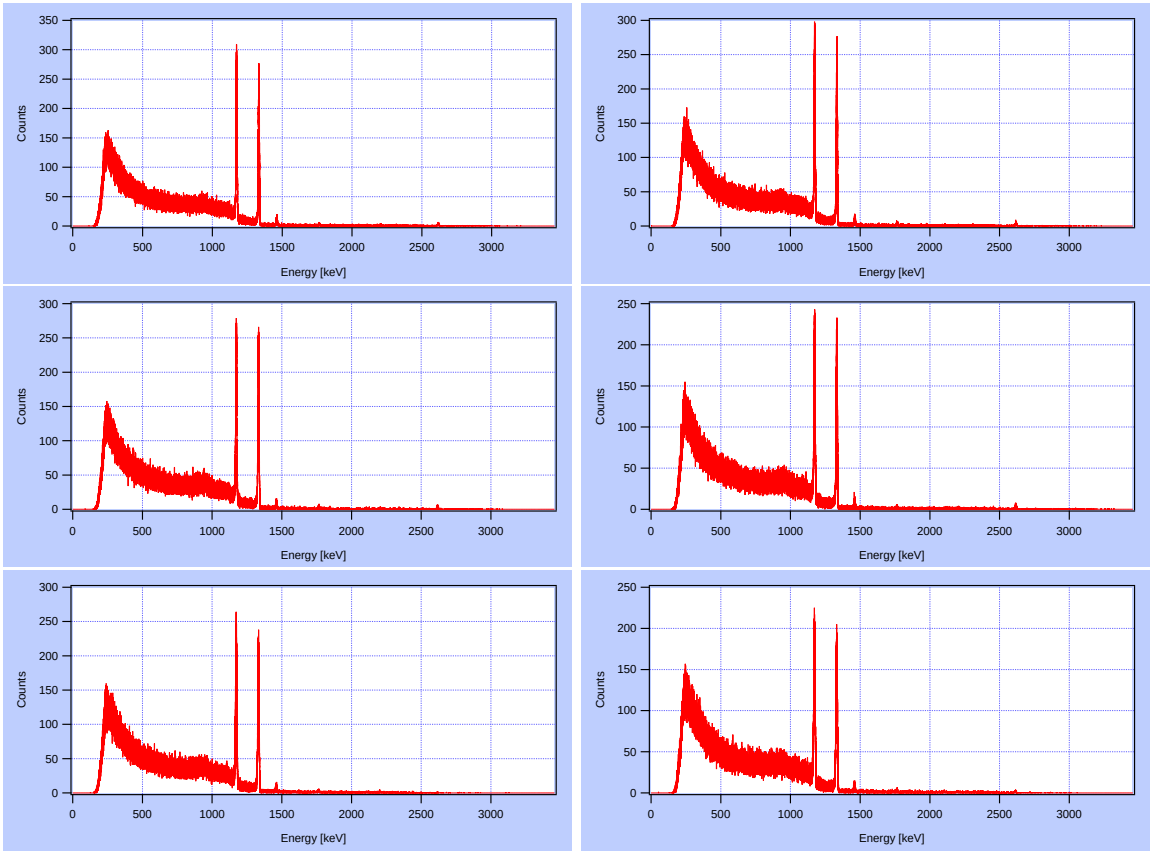

Figure 4.12: ^{60}Co Spectrum starting with current through the 380 nm diode at 0.0 mA (top left), then 0.5 mA (top right), 1.0 mA (middle left), 2.0 mA (middle right), 5.0 mA (bottom left), and finally 10.0 mA (bottom right). With the increase of current through the diode, and accordingly, the increase of the photon flux, the resolution on the ^{76}Ge detector gets worse.

Again, the same effects are evident in these spectra using the 380 nm diode as a blinding effect. As the number of photons which hit the detector are increased, the number of counts of the two gamma-ray peaks decreases and the noise at the lower energy end of the spectrum is increased. Lastly, in the UV range, 360 nm diode was checked to see if it produced the same effects as these two diodes.

Finally, the ^{60}Co spectra using the 360 nm diode as a blinding source are shown in the following figure. For them, the current of the diode was increased to 20 mA since the diode only produces about 1/10 times the amount of photons as the 400 nm.

As can be seen, the same effects are seen with the 360 nm as the two previous diodes. What can also be seen is that the effects of the 360 nm are not as severe as those of the 400 nm and the 380 nm at the same currents running through the both of them. But as determined beforehand, the 360 nm does not emit as many photons as the other two diodes. Therefore, to analyse this data, the same values of photon flux were plotted in the same graph against current.

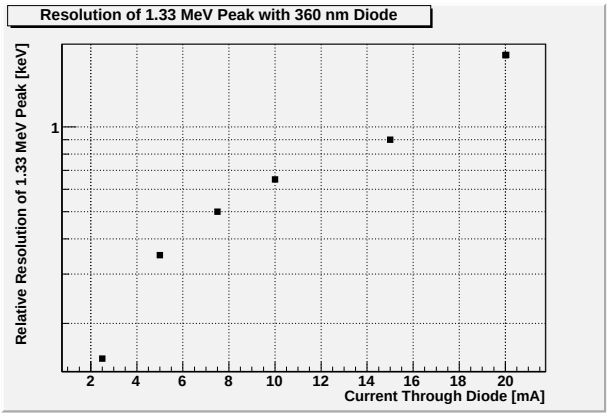

Figure 4.13: This shows the resolution change of the 1.33 MeV peak of the ^{60}Co spectrum as more and more photons are applied onto the detector using a 360 nm diode. The effects of the 360 nm diode are similar to those of the two diodes before. However, the 360 nm diode only produces 1/10th the amount of photons as the 400 nm diode. As more photons are released from the 360 nm diode, the resolution of the measurements gets worse as usual.

What can be seen by Fig. 4.15 is that for the same relative photon flux the detector sees all the diodes the same way. The 400 nm diode has the same effect on the detector as the 360 nm when the same photon flux is applied by both diodes. This shows that the detector is not affected differently by these two wavelengths even though they have different penetration depths inside Germanium. The 360 nm wavelength has a smaller penetration depth, however has the same effect as 400 nm because all the energy is still deposited in the small dead-zone on the ends of the crystal. Even though the photons do not make it into the depleted zone of the crystal, the energy that is deposited still causes leakage current. No electron hole pairs are created when the energy is deposited in this dead-zone. This is the reason for the 360 nm diode creating the same resolution distortion as the 400 nm diode even with a smaller penetration depth; all the energy deposited results in the addition of leakage current.

It follows that there are no other effects on the resolution. The deposition of photons raises the leakage current even if the photons are only deposited on the outside dead zone. Therefore, 120 nm photons, even if they have an extremely small penetration depth, may still cause a rise in leakage current. However, as calculated earlier, the full effects of the 40 000 photons/second from liquid Argon scintillation would not distort the resolution to any magnitudes higher than the picoampère magnitude.

Also of importance is the IR distortion. In our current set-up there is a shield protecting the detector against IR light. This shield is not extremely tight and still allows a miniscule amount of IR light to get in. Even with a small amount of IR photons hitting the detector, the signal is distorted. Any sort of IR light that makes it through the shield will, and by huge magnitudes, distort the resolution on the Ge-detector. Fig 4.16 shows how the detector reacts to a starting amount of IR photons hitting the detector at approximately $1 \cdot 10^8$ per second.

It is seen that the line begins linear, but once there are approximately $1 \cdot 10^{10}$ photons per second, the detector is completely blinded, causing a resolution distortion of 5 keV. This is an extreme distortion and means that if IR light reaches the detector, the measurements would

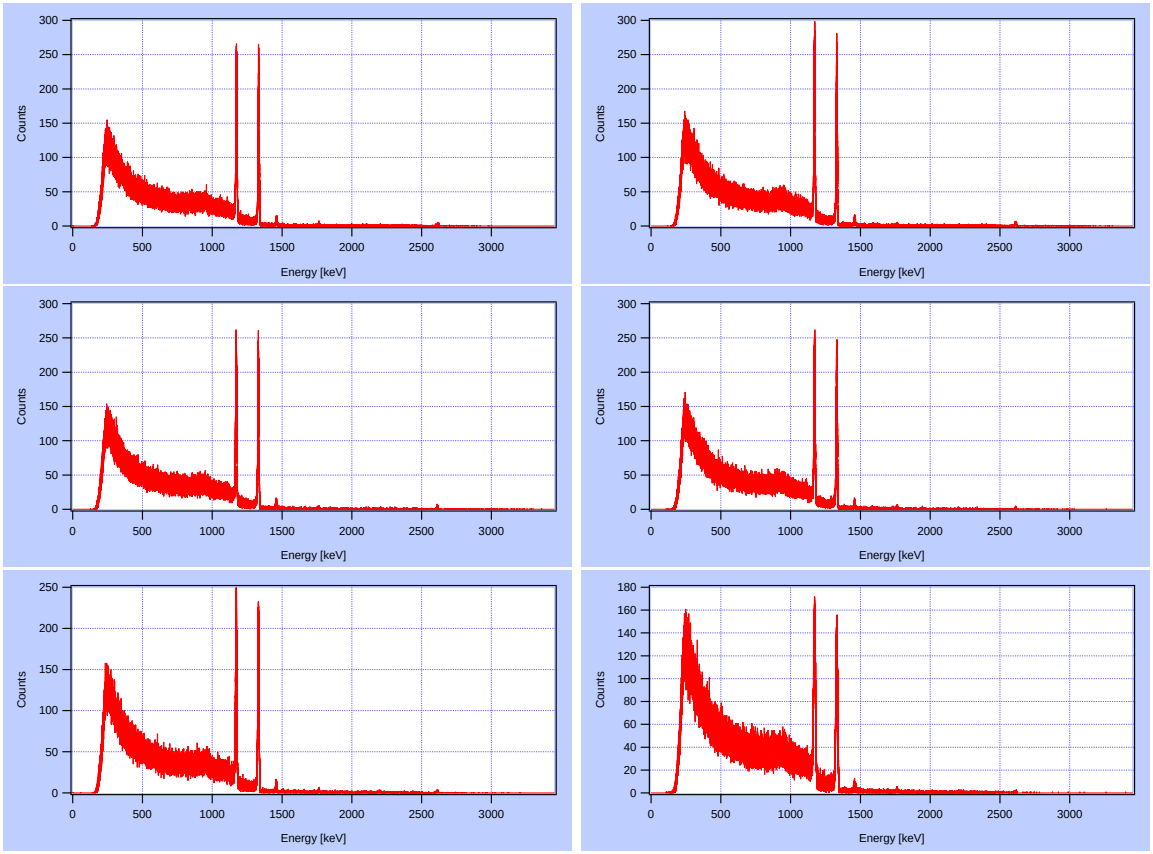

Figure 4.14: ^{60}Co Spectrum starting with current through the 360 nm diode at 0.0 mA (top left), then 3.0 mA (top right), 5.0 mA (middle left), 10.0 mA (middle right), 15.0 mA (bottom left), and finally 20.0 mA (bottom right). With the increase of current through the diode, and accordingly, the increase of the photon flux, the resolution on the ^{76}Ge detector again deteriorates.

have a very bad resolution. This makes it very important to shield the detector from any sort of IR photons, moreso than the UV photons because the penetration depth of IR photons is much higher on the Germanium material. The IR photons create electron hole pairs which drift to the ends of the detector causing such a high rise in leakage current. Once there are enough IR photons hitting the detector and depositing energy, the detector becomes completely blinded since so many drifting electron-hole pairs are created. No measurements can then be made because the detector cannot see anything else other than the IR photons' energy. In Fig. 4.17, the spectra are shown with the different amounts of current running through the diode. It can be seen that the IR photons severely affect the diode and that when the current through the diode reaches 10 mA, which is approximately $1.6{\cdot}10^{12}$ photons/second, the detector is severely blinded and cannot make any accurate measurements.

At first, the LED diodes themselves were tested in order to see their properties. It can be seen that the diodes, other than the 360 nm, had a shift associated with their semiconductor properties. This is expected, the diodes' properties are dependent on temperature. When the temperature drops to 87 K, the energy band gap of the diodes changes and therefore the current going through the diode is slowed. This is one of the reasons for the linear plot jumping out of

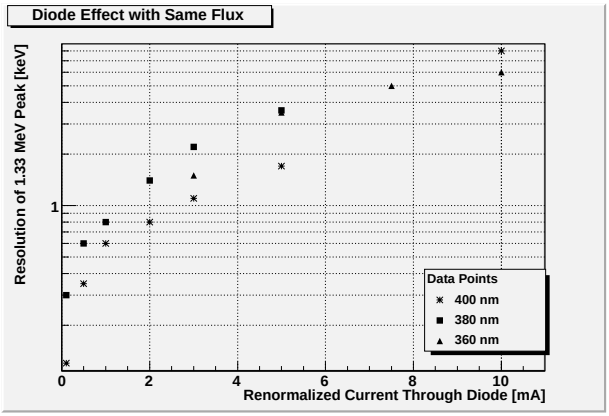

Figure 4.15: This graph shows the Resolution of the detector when approximately same amount of photon flux is emitted from all diodes. It shows they all follow relatively the same linear line. There is no difference in resolution between the 360 nm and 400 nm. The Renormalization of diode current was calculated by multiplying the current determined by the phototransistor Tab. 4.1 by the resolution found at a certain current. This makes all the photon fluxes similar in each diode and allows them to be compared against one another while they each have the same photon flux, and to see how the detector reacts to the different wavelengths at the same photon flux. The background on all spectrum when 0.0 nA was running through the diode was 9.0 keV with a distortion of a maximum of 0.2 keV, which is irrelevant since there is more error on the 9.0 keV. Therefore, when addiding resolution quadratically, the background term was constant for all three diodes at 9.0 keV.

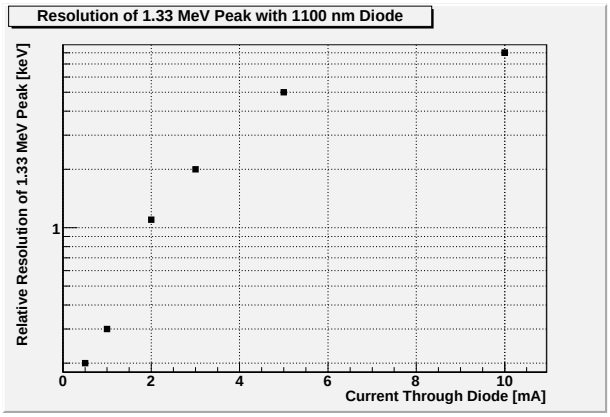

Figure 4.16: This shows the resolution change of the 1.33 MeV peak of the ^{60}Co spectrum as more and more photons are applied onto the detector using a 1100 nm diode. The effects of the 1100 nm diode are similar to those of the three diodes before. However, the 1100 nm diode severly diminishes the accuracy to which other measurements can be made because IR photons blind the ^{76}Ge detector with electron-hole pairs.

its pattern once it hits liquid Argon, seen in Fig. 4.3. Another reason for such an occurance is the fact that electron/hole pairs which are created inside the diode are thermally dependent. When the temperature drops, they have less energy and less occurrance, meaning there is a higher voltage required to make the same current through the diode at 300 K. This explains the similar IV curve shift seen in the first part of the experiment. A final explanation to why the resistance jumps so high when the diode touches liquid Argon is possibly due to the change

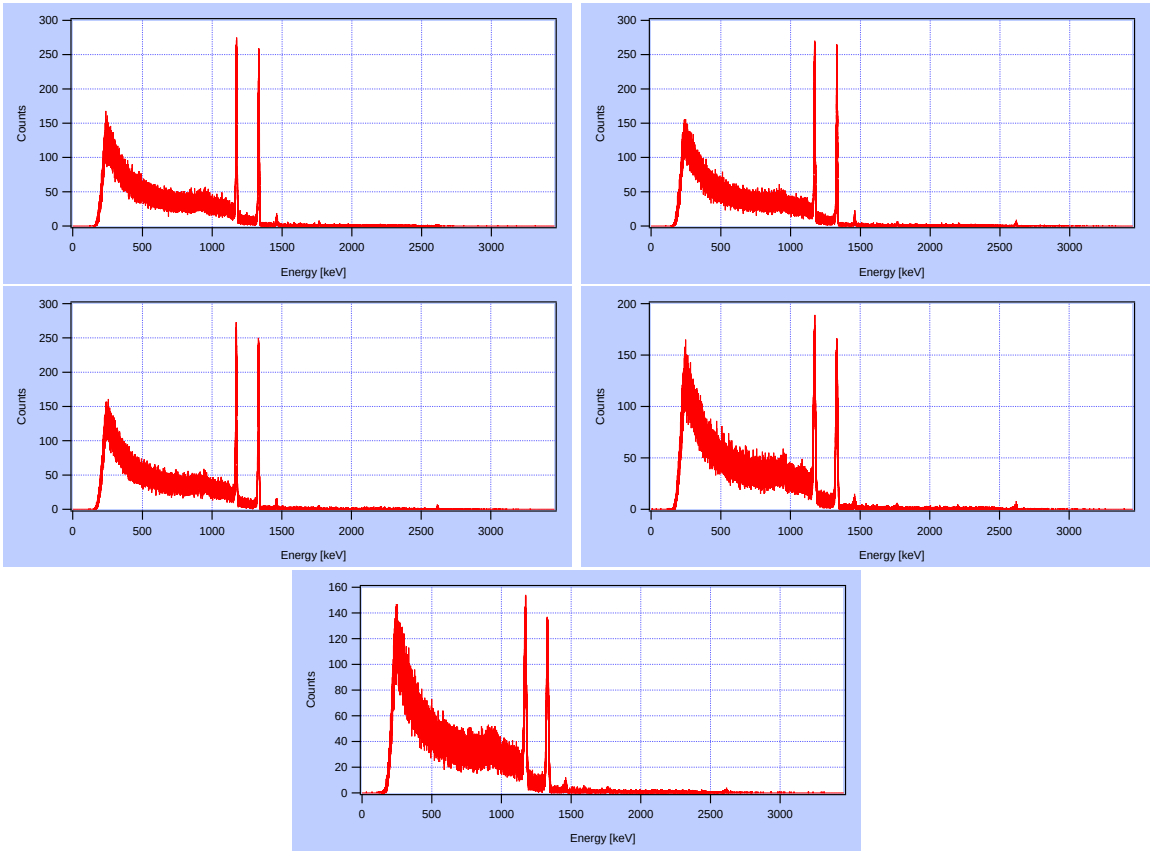

Figure 4.17: ^{60}Co Spectrum starting with current through the 1100 nm diode at 0.0 mA (top left), then 0.5 mA (top right), 2.0 mA (middle left), 5.0 mA (middle right) and 10.0 mA (bottom left). With the increase of current through the diode, and accordingly, the increase of the photon flux, the resolution on the ^{76}Ge detector gets worse. With the 1100nm diode, the resolution gets severley worse and when there are a significant amount of photons hitting the detector, it can be seen in the final spectrum that the peaks have only half the amount of counts as the maximums when no current is running through the diode. There are also a large amount of smaller energy deposition from the IR diode.

in dielectrics if the liquid Argon enters into the diode. If so, this would change the dielectric constant and cause the resistance to rise inside the diode, producing an effect seen in Fig. 4.3. This would explain why it seems temperature has little effect on the plot at higher temperatures just below 300 K. The line remains linear until it touches the liquid, at which point the linearity is broken.

This experiment was done for the purpose of determining whether or not UV photons affect the Ge-detector, and if so, how severely. From what was found, it can be clearly stated that for a large quantity of photons, the detector is affected. As a result, the signal will be distorted. UV photons do affect the detector, however there must be a high number of photons / second, about four orders of magnitude higher photon flux than what is created by liquid Argon scintillization in order to have a severe effect on the detector, at least in the nanoampères range. This means that liquid Argon is safe for use with a Ge-detector since it does not produce enough UV photons to cause a rise in leakage current higher than the picoampères or even femtoampères scales. This means the resolution on the measurements will not change to any significant degree. The reason

why they do not distort the detector as severely as the IR photons is because they do not have the penetration depth in the Ge-detector to make it to the depleted zone of the crystal. The energy deposited by these photons is only left in the dead zone on the edges of the crystal. Therefore no electron/hole pairs are created, just pure leakage current which eventually causes a rise in resolution. The detector can still focus on the energy deposited inside the detector and is only focused on the UV photons when there is a high number deposited on the edge of the crystal. Therefore, liquid Argon scinitllization light will not distort the measurements higher than the picoampères range, but if the number of UV photons is increased, the detector will start to show a worse resolution on measurements made.

For IR photons however, it is found that they blind the detector severely. Even moreso than the UV photons, the IR photons create electron/hole pairs inside the detector which create a leakage current and blind the detector from seeing any other photons or gamma ray energy which would be of potential use for an experiment using the Ge-detector. Therefore, it is strongly advised, if not completely necessary to have an IR shield on the Ge-detector in order to take measurements. Without any shield from the IR photons, it would be impossible to take any measurements with any degree of accuracy.

The background signal found from infrared light also comes in the form of heat. This makes the liquid argon bath for the detector important. Materials supporting the detector should be kept to a minimum to avoid any further unnecessary cause for background on the germanium detector.

4.6 Conclusion

The diodes used in this experiment show expected semiconductor properties which cause a rise in resistance and lowering of current when submerged in liquid Argon. As a result, the diodes can be used to measure the level of liquid Argon and/or liquid Nitrogen if needed for practical reasons.

It is also clear that the Ge-detector does see UV photons, however there need to be a significant amount of photons, about four orders of magnitude higher than expected by liquid Argon scintilation to notice any change in leakage current and change in resolution of the detector. Therefore, the use of liquid argon instead of liquid nitrogen does not change any performance in the detector due to scintillization light. The detector must also be shielded to any IR photons when measurements are made.

This makes the GERDA experiment a very challenging experiment. With such a need for sensitive measurements, the care and protection of the germanium detector is essential for the quality of the results.

5 Muon Tube Analysis

This chapter describes the work done to interface two simulation tools, Geant4 and Garfield, in part for the simulation of the ATLAS muon chambers. This interface was done in order to add measurements such as ionization and electron drift time to gas detector simulations. This was applied to a charged muon traversing through a muon tube to have a better understanding of how a signal is created inside the chamber.

Geant4 [35, 36] is a toolkit which is used to simulate particle interactions and passage through matter, with specific applications in high energy physics. Geant4 can be used to simulate muons traversing a muon tube in ATLAS, however it is unable to simulate the resulting drift of electrons created by ionizations inside the tube.

Garfield [37] on the other hand is a FORTRAN program which is designed specifically for the simulation of drift chambers and gas detectors. This makes it a useful program to use with Geant4 to further the applications and simulation of physics inside a wide range of gas detectors.

It will be described how the first interface has been created between the two simulation toolkits and its application to the ATLAS muon tubes. The extend of the physics of Geant4 will be shown when it is used with the interface to Garfield. Finally, the measurements of the drifting electrons and their signal on the aluminium tube is calculated and shown. The informations is then send back to Geant4 and the interface is complete.

This work has been done with the collaboration from the Institute of Particle Physics in Canada while at the European Organization for Nuclear Research (CERN).

5.1 Geant4 Simulations

Geant4 is a simulation toolkit used to simulate the passage of particles through matter. It has application in many different fields of industry and research, one of them being high energy physics. Geant4 is able to simulate particle interactions with matter and give relevant information about the trajectory of particles, the creation of secondary particles and the energy deposition.

Geant4 has been applied to most of the high energy physics experiments. Its other prime applications are found in the fields of space and radiation, medical technology and technology transfer.

Geant4 was developed to replace Geant3, which was used to model the ATLAS detector for the TDR and technical proposals. Since then, it has been the primary simulation toolkit used for the ATLAS experiment. It can be run in the Athena framework and has been linked to ROOT libraries. [38].

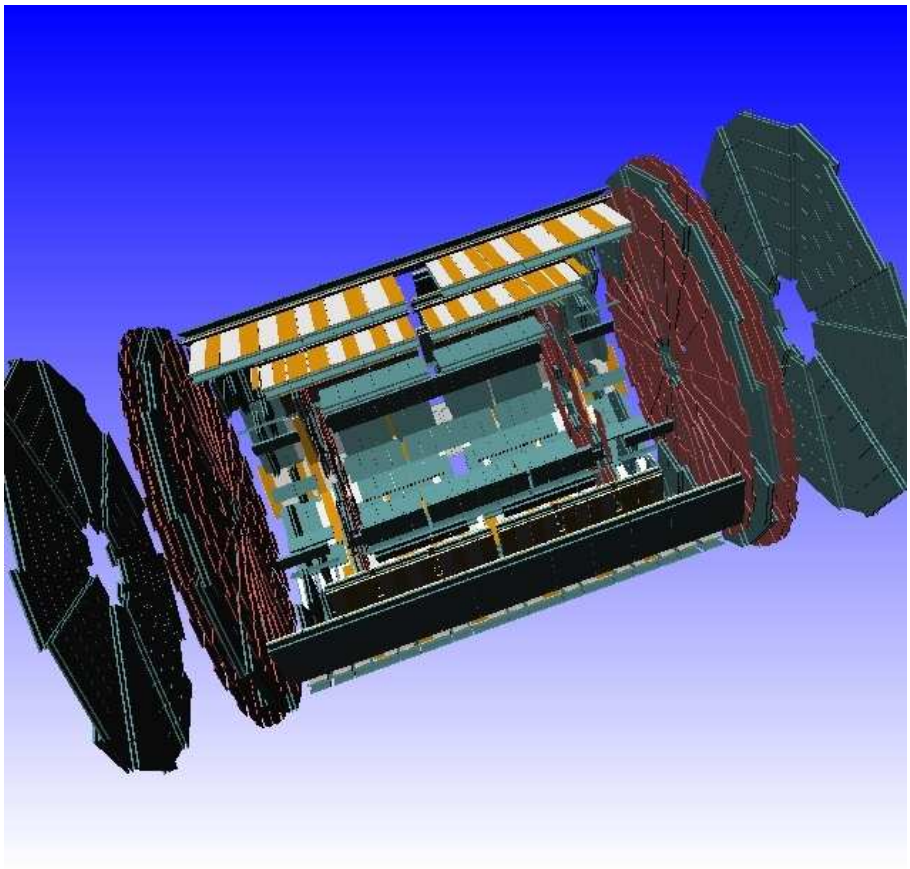

Figure 5.1: ATLAS muon spectrometer simulated by Geant4 toolkit.

Included in the simulation are:

- The geometry and materials of the detector,
- Tracking trajectories of particles,
- Physical processes and interactions,
- Generation of data and storage of events.

A great advantage of the Geant4 toolkit is that it is designed for modern experiments and has a variety of controls, including the interface to other programs. It contains several components such as the event generator, detector simulation, physical interactions, and storage of data which can be tailored to the user's preferences.

For the creation and analysis of the muon tubes, Geant4 is used to:

- create the geometry and material of the detector and physical world volume, defining the boundary of the process,
- initiate the muon particle, its energy, momentum direction, and charge, to launch at the detector,

- create the different gases inside the detector and world volume,
- include all the physical processes such as ionization and multiple scattering inside the detector,
- to determine when a hit on the detector has occurred; thereby determining its position, particle identification, and momentum.

Using the information provided by Geant4, an interface with the Garfield simulation tools allows for a better modelling of the physical process inside the gas detector.

5.2 Garfield Simulations

Garfield is a program which is used to make detailed descriptions of gas detectors, especially drift chambers, time projection chambers (TPCs) and multiwire counters. It is able to create field maps, simulate the drift of electrons and the simulation of induced signals.

However, three dimensional solutions for fields are non-trivial, most of which are not solved analytically. Therefore Garfield uses other finite element programs such as Maxwell [39], tosca [40], QuickField [41] and FEMLAB [42] for its calculations. This is also due to the complexity of dielectric media and other electrode shapes, which are difficult to be treated with just analytic techniques.

This makes Garfield a very powerful program at treating gas detectors and fields inside gases. Its interface with Magboltz [43], a program which designs the gas and all the internal fields, allows for the computation of most electron transport properties. This can be done for arbitrary gas mixtures. This is used for the treatment of large gas detectors, and has special applications in the simulation of the ATLAS muon tubes. Therefore interfacing this program will allow Geant4 access to physical processes such as:

- field maps for fields as well as contour plots in two and three dimensions,
- compensation in fields and signals due to wire sag in detectors,
- calculation of drift parameters of electrons and ions, specifically drift time and drift plots,
- determination of a signal induced by the charged particles as they move through the detector, with the inclusion of factors such as “delta-electrons”, diffusion, and electron pulse.

5.3 Interfacing the Simulation Programs

To run Geant4 and Garfield simultaneously, the libraries between the two programs must be linked. This is the first attempt to interface Garfield with Geant4. The first important step is to manage the correct libraries from each program. The libraries required to run the interface are: Geant4, CLHEP, Garfield, and ROOT. Though ROOT libraries are not essential, they are needed for any visualization of the simulation.

Not all of the versions for these four programs are compatible. Geant4 requires the proper libraries from CLHEP in order to run any task. For ROOT to be added, version 5.10.00 is the one used in this example. The choice of CLHEP and Geant4 is not important as long as they are compatible with each other.

The next stage in interfacing the two programs comes from linking the shared libraries in the makefiles. This needs to be done with care for different versions, 64 or 32 bit computers. However this must stay consistent in both makefiles. This is the same for the compiler used. Garfield is a FORTRAN program and needs g77 to compile properly.

The next step is to add the proper files. The simulation needs to have a class which links the two programs together. For this example this class is given the name `garftube`. The `garftube` class is called from inside Geant4 and uses other Garfield specific classes to make its analysis. The flow chart is found in Fig. 5.2. For the current example, the method `Process Hits` inside Geant4 calls `garftube`.

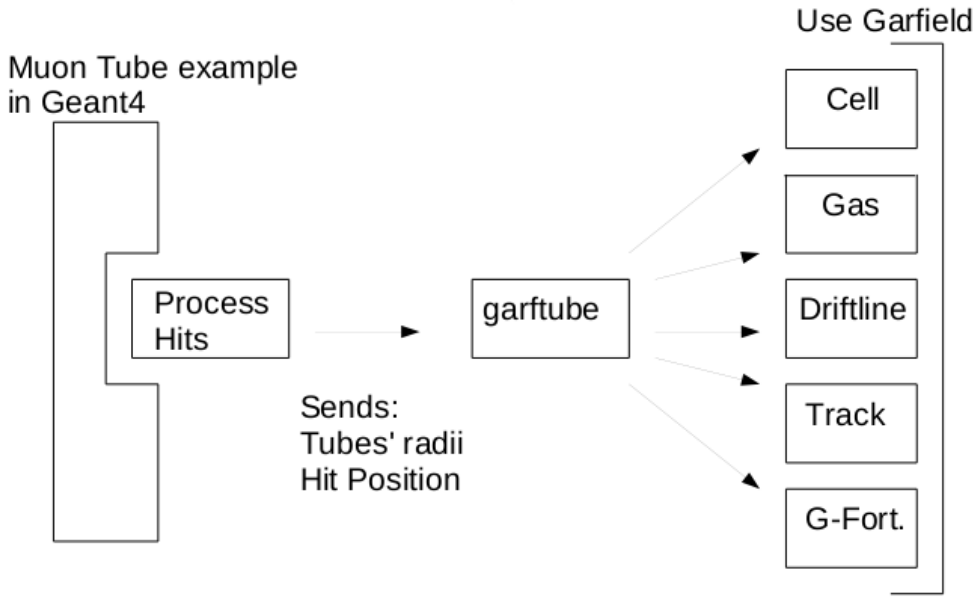

Figure 5.2: Flow chart for the first prototype interface, which calls Garfield properties in the Geant4 method *Process Hits* of our muon tube example.

Therefore all of the classes from Garfield, along with the ROOT libraries must be added to the regular Geant4 makefile. After compiling these garfield classes, their output is added to the makefile of the Geant4 example. This is done as follows.

In the GNUmakefile of the example in Geant4:

```
ifdef ROOTSYS
CPPFLAGS += $ (shell $(ROOTSYS)/bin/root-config --cflags)

ROOTLIBS = Tube/garftube.o Tube/plotlib.o Tube/garfieldfortran.o
```

```
            Tube/garfieldalgebra.o  Tube/garfieldfield.o
            Tube/GarfieldGraphics.o Tube/Cell.o Tube/Driftline.o
            Tube/Track.o Tube/Gas.o
            $(shell $(ROOTSYS)/bin/root-config --glibs) -lMinuit
            -lHtml $(shell cernlib kernlib, mathlib,packlib) -lg2c
ROOTLIBS := $(filter-out -lNew,$(ROOTLIBS))
ROOTLIBS := $(filter-out -lThread,$(ROOTLIBS))
ROOTLIBS := $(filter-out -lpthread,$(ROOTLIBS))
LDLIBS +=$(ROOTLIBS)
endif
```

This is the core of the linking procedure. This brings all of the libraries together in the Geant4 makefile. From here, Geant4 can run an example without separately using Garfield for analysis. Geant4 now adds all of the Garfield libraries it needs for gas detector analysis. Next, an example is constructed in Geant4 to show how this process works. This is the first prototype of its kind.

5.4 Muon Tube Set-up and Run Action in Geant4 using Physical Applications from Garfield

To begin the Run Action, the detector construction is written in Geant4. The Run Action is the physical process which uses a particle gun to simulate a single particle directed towards the detector. The energy of the incoming particle is controlled, along with its initial direction from Geant4 before the run begins.

The particle simulated for the analysis is a positively charged muon with an incoming energy of 10 GeV, about what should be expected from muons produced at the LHC. They begin at the world volume boundary, shooting through the detector. Geant4 is able to track the particle through the designated physical boundary and into the detector.

The detector is rotated 90 degrees so that the particle will hit the tube perpendicular to the long end. From this point of entry, the class garftube is called which uses Garfield physical applications. The return of information is sent back to the Geant4 example and the muon is tracked by Geant4 until it reaches the boundary of the world volume.

5.4.1 Detector Construction

For the analysis of the muons, the detector constructed is that of the ATLAS muon tube. The first object which is created is the world volume. This is the area in Geant4 at which our physical process will occur. It defines the physical boundary at which all of the physics will be recorded.

The creation of the objects, in this case the muon tube detector, is done in two phases. The first is the establishment of the logical volume. The second is the creation of the physical volume, which creates the physical attributes of the logical volume. The world volume is filled with normal room condition air.

The detector itself is made of a gas of 93 % Argon and 7 % CO_2 just as in the ATLAS muon spectrometer. It is held at 25 °C and at a pressure of 3 atm. The detector is constructed with an outer radius of 1.5 cm. In the centre of the Tube runs an Al wire with an outer radius of 30 μm. This information is all created in Geant4 and can be visualized from Geant4 control as in Fig. 5.3.

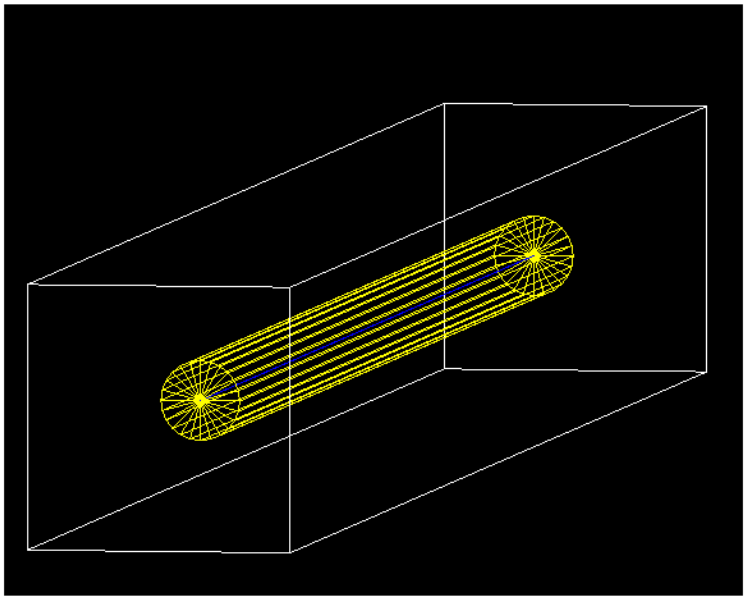

Figure 5.3: Atlas Muon Tube constructed in Geant4 and visualized by OPENGL.

Now that our detector is constructed in Geant4, it must also be properly created in garftube from Garfield. Since all the hit parameters will be passed during the simulation, the gas must be created beforehand for ionization purposes. It is created by Magboltz, seeding the gas and HEED model for ionizations which will be described in detail later.

5.4.2 Gas in Detector

The gas in the simulated detector is constructed in Geant4, however it does not have the capabilities to analyse the electrons in the muon tube. Therefore, for the analysis, Garfield is also used to create the gas inside the tube. This is done using Magboltz 7.1 which creates a gas mixture of 93 % Argon and 7 % CO_2.

This process must be done separately in a gas file. This gas file is created ahead of time by the interface with Magboltz which creates all the parameters of the gas given the structure and size of the detector. Using this information, it produces all of the properties of the fields numerically and stores them to a file. This procedure takes several hours and is needed to be completely ahead of the simulation.

5.4.3 Run Action

The Run Action, is started by creating the detector from all the set parameters. Geant4 sets and describes the detector and the surrounding world volume by its list of properties and physical processes. Once the detector has been constructed, Geant4 then begins by shooting the muon at the detector.

The muon traverses through the Geant4 world volume until it reaches the muon tube, which is defined as the sensitive detector. This sensitive detector is the region in which Geant4 records hits. When a particle hits the sensitive detector, it is stored in memory. As the hit is being processed by Geant4, the physics of Garfield is used. This is done by calling the `garftube` class which uses the physics of Garfield.

Once the call to this class has been completed, with each step in the sensitive detector, the muon continues traversing, into the world volume after the sensitive detector until it reaches the boundary of the world volume. This boundary stops the run action and collects all the information from the event. An event which has been created for the muon tube is shown in Fig. 5.4. The trajectory of the muon traversing through the world volume and into the sensitive detector can be seen by the red line.

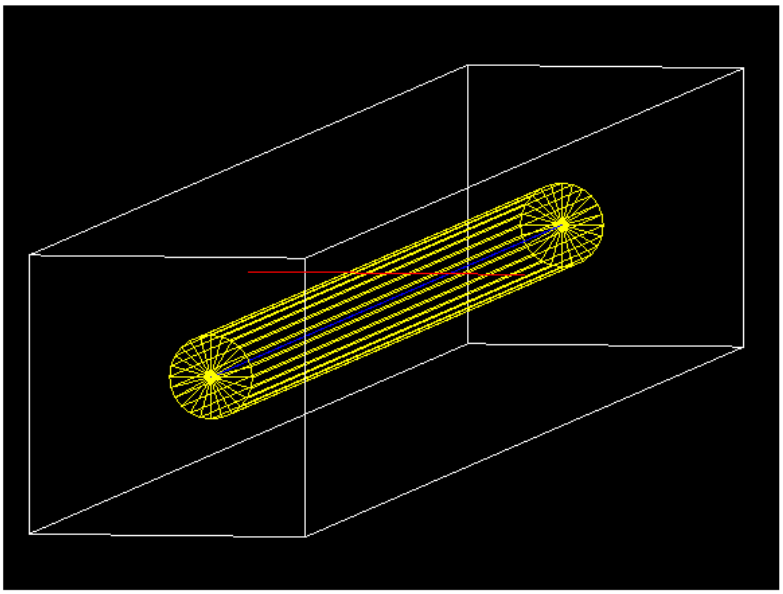

Figure 5.4: The world volume containing the event of a 10 GeV muon traversing through the muon tube. The call is made to garftube when the muon is inside the sensitive detector, defined by our muon tube.

The call for the `garftube` class is made upon hitting the sensitive detector in the `ProcessHits` method as follows:

```
#include <vector>
```

```
#include "/afs/cern.ch/user/g/guindon/GEANT4/Tube/garftube.h"

G4bool ExN02TrackerSD::ProcessHits(G4Step* aStep,G4TouchableHistory*)
{

...

G4ThreeVector v1;
G4ThreeVector v2;
v1 = aStep->GetPreStepPoint()->GetPosition();
v2 = aStep->GetPostStepPoint()->GetPosition();
G4double x1tem = v1.getX();
G4double y1tem = v1.getY();
G4double z1tem = v1.getZ();
G4double x2tem = v2.getX();
G4double y2tem = v2.getY();
G4double z2tem = v2.getZ();

double drifttime = garftube(fRadius,fRadius2,x1tem,y1tem,z1tem,x2tem,y2tem,z2tem);
printf("The 10th electron arrives at %g.\n", drifttime);
return true;
}
```

In this procedure, firstly the pre and post step positions are determined by Geant4. These points are the intial and final position of the muon in the sensitive region. Each position is recorded according to our world position and it is passed through the argument of the call to garftube.

The other two variables passed in the argument are fRadius and fRadius2. These are the radii of our muon tube and Al tube respectively. These variables are passed to allow an arbitrary volume to be created in Geant4. Therefore any detector can be passed along with any entrance and exit point. All of these parameters are used by our class garftube for physics inside the muon tube, such as drift time and velocities which would otherwise be impossible using only Geant4 physical properties.

The class garftube also returns a double term, denoted here as drifttime. This drifttime is the signal time on the trigger. It is used to simulate the time it takes for the avalanche of electrons on the wire to induce a signal. This value can be further used in Geant4 for other applications. How this is done in the class garftube will be described in the next section.

5.5 Muon Tube Studies

This analysis uses the transport properies of the gas inside the tube and calculates the electron transport due to ionizations from the muon. The drifting electrons are tracked and collected in the signal process. These physical descriptions are all possible with the first interface between Geant4 and Garfield.

5.5.1 Physics using Garfield Capabilities

As the muon passes through the muon tube, it causes ionization of the gas, resulting in electrons being produced. For this simulation, the HEED model for ionizations is used. The HEED model produces ionizations randomly. They are randomly spaced with random energy. The garftube class records the ionizations created by the muon and traces them based on the electric field inside the tube.

An electric field is created inside the tube by Garfield. The electric field as a function of radius in the muon tube is shown in Fig. 5.5.

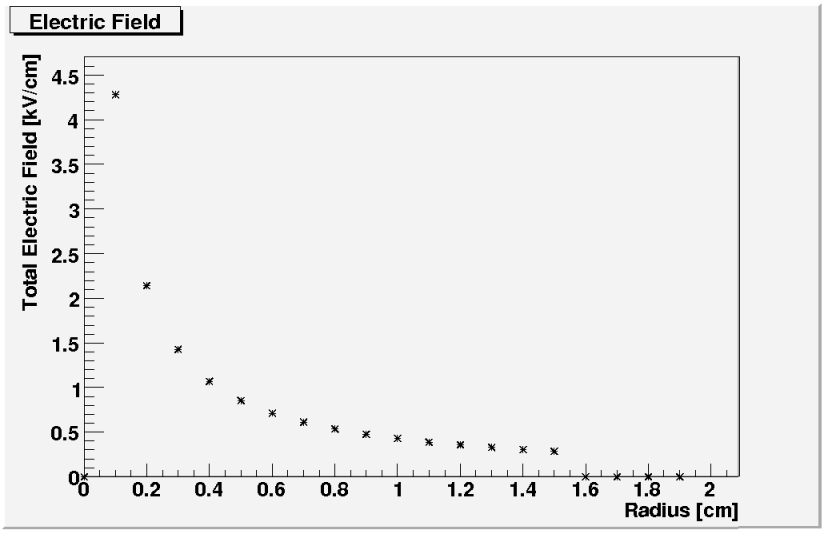

Figure 5.5: Electric field inside the muon tube as a function of the radius. It can clearly be seen that the electric field ends at the boundary of the tube with a radius of 1.5 cm.

The electric field inside the tube is strongest at the centre of the tube, along the Al wire. As it is further from the centre, the electric field diminishes and this property has an effect on the drift of the electrons. This is calculated after the ionizations of the electrons.

5.5.2 Simulating the Ionizations

The ionizations in the muon tube are created by the HEED method. This traces the track of the muon and places ionized electrons along the path with various energies. The ionized electrons begin to drift from their position according to the electric field. This can be seen in Fig. 5.6.

Due to the electric field created in the tube, the electrons drift to the centre of the tube, the Al wire. Due to the drifting electrons, a signal is created at the wire. The signal allows the determination of the distance from the wire to the muon.

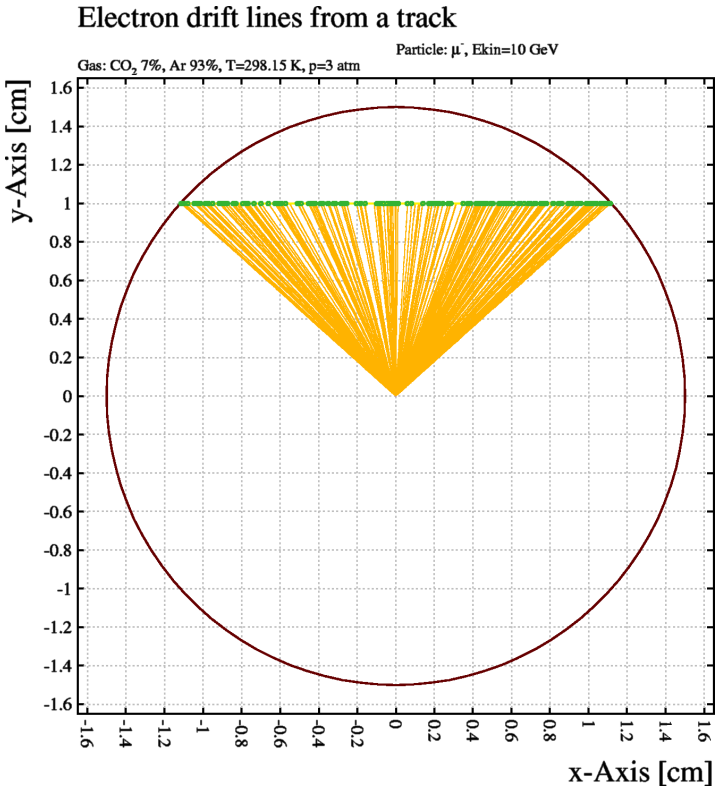

Figure 5.6: Electrons due to ionization are created along the path of the muon. This is the horizontal line across the top of the tube. They drift according to the electric field, leaving a path of lines in yellow.

From the diagram it can easily be seen where the muon entered and exited, however this is not possible in the ATLAS muon tube. What must be done is a calculation of the time on the signal. From this, one is able to tell how far away from the wire the muon passed through the tube. With the hit of 20 muon tubes on average per muon, the exact position can be triangulated. This makes it important to study the drift parameters and to understand how the electron is drifting inside the tube.

5.5.3 Calculating Drift Velocities

It is possible to study the drift velocities of the electrons inside the gas using Garfield. Once the electrons have all arrived at the wire, the time it took them to drift towards the electrode can be calculated. This is done for different segments of the detector. The transport properties of the gas can be calculated due to the known electron mobility.

From measurements of the electron mobility, the velocity of the electrons can be seen for different magnitudes of electric field. For a gas of 93 % Ar and 7 % CO_2, the drift velocity of the electrons can be plotted against the electric field. This is shown in Fig. 5.7.

The first thing to note from the graph is that it is not linear. The electric field can be represented in terms of electron energy. At an electric field between 10^3 and 10^4 V/cm, there is a dip in the velocity of the electrons. It corresponds to a decrease in the velocity for a given

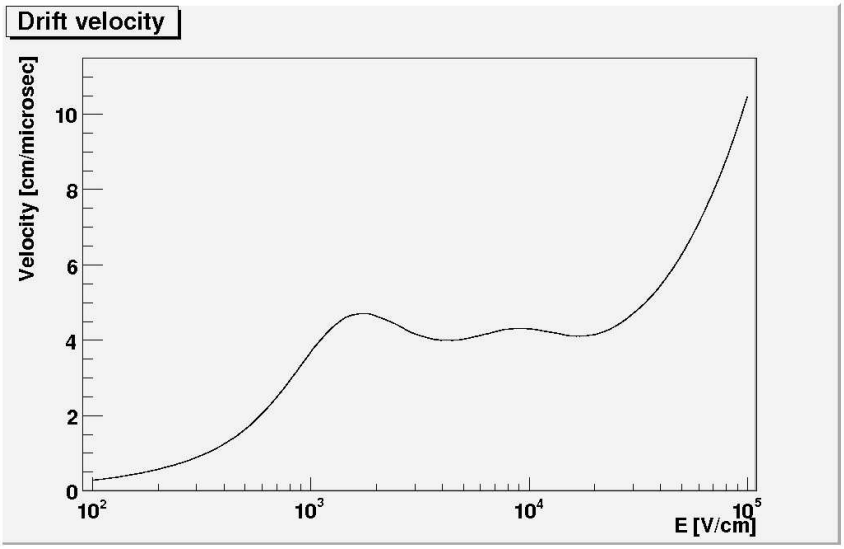

Figure 5.7: Drift Velocity of the electrons inside the gas of the ATLAS muon tube. It is interesting to note the plot does not show a linear relationship, yet is dependent on quantum effects from the gas.

increase in the electric field. This does not seem obvious. However, if the electric field could be translated into the electron energy it would coincide with about 0.2 or 0.3 eV.

Looking at the properties of Argon, the cross-section for Argon as a function of energy in eV is given in Fig. 5.8. It can be seen that at the energy of 0.2 and 0.3 eV there is a large decrease in the cross section. This coincides exactly with the decrease in drift velocity of the electrons at certain places in the strength of the electric field.

The reason for such a dip in the cross section is due to the phase shift in the wavefunction of the electron [44]. This minimum is known as the Ramsauer minimum. As the electron approaches, it undergoes an S-wave phase shift of π due to a strong attractive force with the argon nucleus. At this point, the cross section is smaller and thus, the electrons at this electric field will drift slower. The same effect can be seen in CO_2, however the effect is much slower. This is also seen in Fig. 5.8.

The Ramsauer effect was first discovered in 1921 and was one of the first quantum effects to be observed and published [45]. It was later published by J.S. Townsend and V.A. Bailer [46] and therefore it is also known as the Ramsauer-Townsend effect.

This effect is not only limited to Argon, but the heavier Noble gases all have a similar effect at progressingly higher energies. In the heavier noble gases such as Krypton and Xenon it occurs at 0.5 eV and 0.65 eV, respectively.

5.5.4 Calculating Drift Time

For the measurement in gas detectors the drift time is an important measurement for signal analysis. The location of the traversing muon can thus be determined. The drifting is used to

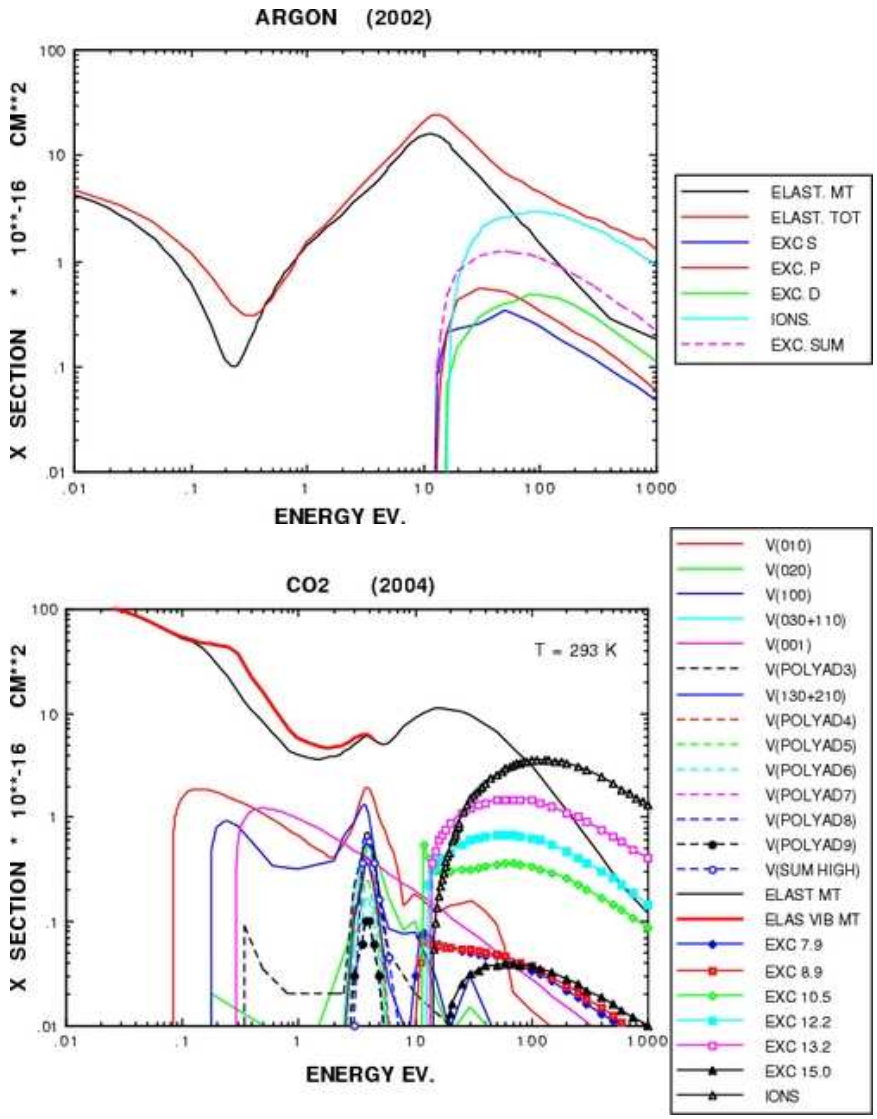

Figure 5.8: Cross Section of argon and carbon dioxide as a function of energy. These graphs are taken from the Magboltz 7.1 database for gas properties.

understand how the electrons propogate in the gas and to see from where the resulting signal originates.

The drifting electrons are due to ionization of the gas which creates the primary and secondary electrons. These electrons then drift according to the electric field and diffusion properties. In the ATLAS muon tube, they drift towards the Al wire where the signal arrives with a certain time delay from the muon entering the tube.

During the drift of the electrons, there are also processes which affect the time. One of these processes is diffusion. Due to diffusion, some electrons arrive quicker and some slower. This is simulated by Garfield and taken into account in the present muon tube example. Fig. 5.9 shows the different drift times of the electrons according to their location along the distance from where the muon entered the tube.

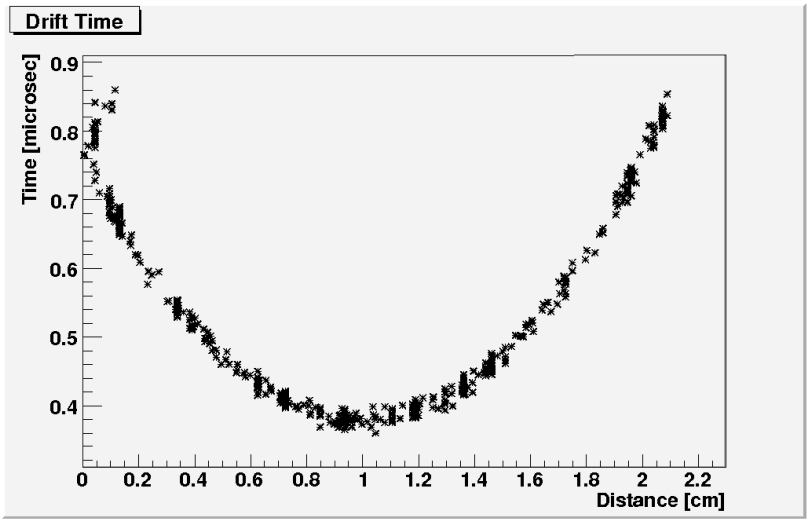

Figure 5.9: Drift time of the electrons from across the track of the muon. The distance along the bottom represents the distance of the muon in the tube. Therefore, 0 cm corresponds to the entrance and 2 cm corresponds to the exit. The quickest electrons to arrive are the ones created closest to the Al wire, the centre of the track inside the tube. The calculation also takes into account diffusion.

5.5.5 Trigger Time back to Geant4

The simulation of the signal which the Al tube registers is done in `garftube`. This is done to allow users access to the trigger time for further applications in Geant4. The trigger time is the time by which a signal is seen in the muon detector, starting when the ionization was created. To do this simulation, all of the drift times are calculated using Garfield. Instead of storing all of them in memory due to huge file sizes and long calculation times, a vector is used to calculate the signal.

To do this, the tenth electron to reach the Al wire is found by checking all of the values of the drift time. The time of the tenth electron is the time deemed for the signal to trigger. This is due to electronic noise and other delays in the electronics. This is a very realistic simulation of the time for the signal from the drifting electrons due to the delay in the electronics.

This time for the triggering of the signal in the tube is then recorded in the class `garftube` and is returned to `ProcessHits`, the method inside Geant4. From here this number can be used in Geant4 for purposes of the user. This completes the interface and demonstration for the ATLAS muon tube.

5.5.6 Muon Measurements per Bunch Crossing and Timing of Interface

The outer most part of the ATLAS detector is made up of the muon detectors. Since the muon is a minimum ionizing particle, it is able to escape the inner detector and calorimeter.

Therefore, the muon spectrometer is put on the outside of the detector to identify the muons created in ATLAS.

The muon detector is composed of 400 000 tubes as stated earlier. To study the simulations of events in ATLAS, the amount of muons produced per event needs to be understood to make proper accounts for timing of the simulation.

In one bunch crossing at ATLAS, an average of 25 protons are accelerated in opposite direction of another 25 protons. Per bunch crossing, on average, about 20 events will occur [47] from the collision of the two bunch crossings. From these 20 events, about 1 muon will be created on average. Most likely it will not reach the muon tubes due to insufficient energy. This leaves the number of muons reaching the tubes to be very low, much lower than 1 per bunch crossing.

If however, a muon does reach the tubes, it will hit about 20 tubes as it traverses outwards from the interaction point. For simulation purposes, this means that the simulation time must be able to handle between 20 and 100 tubes being hit out of 400 000 per 25 ns to be sure the timing is sufficiently fast.

5.6 Conclusion and Outlook

The first prototype design for interfacing Geant4 with Garfield has shown to be very useful for simulating large gas detectors. The interface adds physical properties of events inside gas detectors. This would otherwise not be possible with only Geant4. It allows Geant4 to make calculations of gas detectors without using a secondary simulation.

The applications of Garfield go further beyond just the muon tube example. So far, drift properties of the electrons have been calculated. But also the properties of the gas of the detector can be clearly shown using Garfield.

The next application being sought after is the generalization of this first prototype to other models. One example already being pursued by TRIUMF in Vancouver, Canada, is the application of this prototype to time projection chambers. This has applications in particle simulations of ALICE, and the ILC development.

One field which is of particular interest to many is the avalanche effect. This occurs in the muon tubes, and other gas detectors, as the electrons approach the Al wire. The number of electrons increases with the increase of the electric field. Garfield can take this into account and this can be added to the simulation for an even more advanced description of the drifting of the electrons. This can be done with the addition of a method in `garftube`.

Other additions to the first prototype are also being looked at by members of the Geant4 Collaboration at CERN. Further additions to the calculation of the signal in the Al wire can be done. Another attempt is to add many muon tubes in one simulation. Another area which could be looked into is to call `garftube` at every step in the sensitive detector. This code only gives the entrance and exit coordinates of the sensitive detector. This will allow a step by step

calculation of drift times as the muon makes trajectory steps across the detector. It will also make better trajectories with respect to external magnetic fields.

This protoype is also a test of CPU time for such a process. As mentioned previously, the number of muons, which hit the muon spectrometer per bunch crossing is much less than one. However, if it is to be assumed that one muon reaches the muon spectrometer which is created per bunch crossing, it would hit about 20 tubes. If the computer is to call the garftube class each step in approximately 20 sensitive detectors out of 400 000, this calculation would be sufficient. This shows not only the ability of Garfield to calculate field maps and drift parameters with impecable accuracy, but with also an irrelavent amount of time.

All of these additions will help improve simulation of gas detectors with Geant4. This interface will vastly increase the usefulness of an already very widely used toolkit. It will allow for a whole new branch of physical simulations via Geant4 and will help in the design and study of the future International Linear Collider (ILC).

6 Conclusion and Outlook

In the study of the neutrino physics detector, a p-type Ge-detector for the GERDA experiment was studied while being operated in a dewar filled with liquid Argon. The influence of IR- and UV-light on the detector was studied with a set of LEDs. The properties of the diodes were measured while submerged in liquid Argon. Once they have been determined, it was found that some did not behave as expected. As a result, the test stand was adapted to one in which the lights remained outside the dewar, but still managed to shine onto the detector.

The UV-wavelengths of 360 nm, 380 nm, and 400 nm were tested on the detector. The addition of photons from all three UV-wavelengths resulted in degredation of the detector's energy resolution. No differences between the wavelengths' effects on the detector were noticed when the photon flux was normalized.

The IR-wavelength of 1100 nm was also tested to check how the detector reacts to IR background sources. The IR-wavelength showed the same distortion in the resolution as the UV-wavelengths did. This shows the importance to limit the background on the p-type Ge-detector.

It was shown that the photon flux hitting the detector showed drastic resolution changes. However, this photon flux is much higher than would be expected from liquid Argon. From the measurements, it has been shown that the photon flux of Argon is too small to cause any noticeable effect on the detector. Thus, liquid Argon is a suitable candidate to operate the Phase I detectors in for the GERDA experiment.

In the second part of the detector studies, a protoype interface was created to link Geant4 with Garfield. This interface links the libraries of CLHEP, Geant4, Garfield and ROOT. This adds the simulation capabilities of Garfield to Geant4, in particular the ability to describe fields in gas detectors, to measure ionization and calculate the drift of the resulting electrons.

As an example, this was shown for the ATLAS muon tube. The geometry was created in Geant4 and passed through the arguments of the class `garftube`. This class uses the gas description capabilities of Garfield. For the muon tube, it calculates the ionization, and then drifts the electrons according to the electric field. It then tracks each electron until it reaches the Al wire. From this, the drift velocity and time are calculated. This is of use in calculating trigger signals induced by the current. The final process which occurs in `garftube` is the calculation of the induced signal. This information is returned back to Geant4 for the user.

The program is also fast enough to be called in every step of the detector. This is due to the fact that only about 20 out of 400 000 muon tubes are hit by a muon per bunch crossing. One simulation itself takes an unmeasureable time. Therefore, this first prototype can be used for the total ATLAS muon spectrometer. Further applications are, e.g., gas detectors for the ILC.

Bibliography

[1] S.L. Glashow, *Partial Symmetries of Weak Interactions*, Nucl. Phys. **22** (1961) 579.

[2] S. Weinberg, *A Model of Leptons*, Nucl. Phys. **19** (1967) 1264.

[3] A. Salam, *Weak and Electromagnetic Interactions*, exerpt from: W. Svartholm, editor, *Elementary Particle Theory*. Stockholm (1968), Almquist and Wiksell, 1968 367.

[4] P. W. Higgs, *Broken Symmetries and the Masses of Gauge Bosons*, Phys. Rev Lett. **13(22)** (1964) 508.

[5] G. S. Guralnik, C. R. Hagen, and T. W. B. Kibble, *Global Conservation Laws and Massless Particles*, Phys. Rev Lett. **13(20)** (1964) 585.

[6] R. J. Davis, D. S. Harmer and K. C. Hoffman, *Search for neutrinos from the sun*, Phys. Rev. Lett. **20** (1968) 1205.

[7] B. T. Cleveland et al., *Measurement of the solar electron neutrino flux with the Homestake chlorine detector*, Astrophys. J. **496** (1998) 505.

[8] P. Anselmann et al. [GALLEX Collaboration], *Solar neutrinos observed by GALLEX at Gran Sasso*, Phys. Lett. B **285** (1992) 376.

[9] M. Altmann et al. [GNO Collaboration], *GNO solar neutrino observations: Results for GNO I*, Phys. Lett. B **490** (2000) 16.

[10] J. N. Abdurashitov et al. [SAGE Collaboration], *Measurement of the solar neutrino capture rate by SAGE and implications for neutrino oscillations in vacuum*, Phys. Rev. Lett. **83** (1999) 4686.

[11] Y. Fukuda et al. [Kamiokande Collaboration], *Solar neutrino data covering solar cycle 22*, Phys. Rev. Lett. **77** (1996) 1683.

[12] J. Hosaka et al. [Super-Kamkiokande Collaboration], *Solar neutrino measurements in Super-Kamiokande-I*, Phys. Rev. D **73** (2006) 112001.

[13] Q. R. Ahmad et al. [SNO Collaboration], *Direct evidence for neutrino flavor transformation from neutral-current interactions in the Sudbury Neutrino Observatory*, Phys. Rev. Lett. **89** (2002) 011301.

[14] C. Weinheimer et al., *High precision measurement of the tritium beta spectrum near its endpoint and upper limit on the neutrino mass*, Phys. Lett. B **460** (1999) 219.

[15] V. M. Lobashev et al., *Direct search for mass of neutrino and anomaly in the tritium beta-spectrum*, Phys. Lett. B **460** (1999) 227.

[16] A. Osipowicz et al. [KATRIN Collaboration], *KATRIN: A next generation tritium beta decay experiment with sub-eV sensitivity for the electron neutrino mass*, arXiv:hep-ex/0109033.

[17] NuMass collaboration, URL site at: http://www.hep.umn.edu/numass .

[18] J. Pumplin, D. R. Stump, J. Huston, H. L. Lai, P. Nadolsky and W. K. Tung, JHEP **0207** (2002) 012.

[19] W. M. Yao et al. [Particle Data Group], *Review of particle physics*, J. Phys. G 33 (2006) 1.

[20] ICRU Report No. 49, *Stopping Powers and Ranges for Protons and Alpha Particles*, (1993).

[21] D. E. Groom, N. V. Mokhov, and S. I. Striganov, *Mass-Ratio Method Applied to the Measurement of L-Meson Masses and the Energy Balance in Pion Decay*, Atomic Data and Nuclear Data Tables **78(2)** (2001) 183.

[22] S. Schönert et al. [GERDA Collaboration], *The GERmanium Detector Array (GERDA) for the search of neutrinoless beta beta decays of Ge-76 at LNGS*, Nucl. Phys. Proc. Suppl. **145** (2005) 242.

[23] The LHC Machine Group reported by G. Brianti at the XVth Interm. conf. on High Energy Accelerators, Hamburg, Germany, *Status report on the CERN Large Hadron Collider (LHC)*, (1992), CERN/AC-DI/92-03 (LHC).

[24] The ALICE Collaboration, *Technical Proposal for A Large Ion Collider Experiment at the CERN LHC*, (1995).

[25] The LHCb Collaboration, *LHCb Technical Proposal*, (1998).

[26] The CMS Collaboration, *CMS Physics Technical Design Report - Volume I*, (2006).

[27] The ATLAS Collaboration, *ATLAS Detector and Physics Performance Technical Design Report - Volume I*, (1999).

[28] ATLAS Inner Detector Community, *ATLAS Inner Detector Technical Design Report*, (1997).

[29] The ATLAS Collaboration, *Liquid Argon Calorimeter Technical Design Report*, (1996).

[30] Oliveira Damazio, Denis on behalf of the ATLAS Collaboration. *ATLAS LAr Calorimeter: Construction, Integration, Commissioning*, Journal of Physics: Conference Series **110** (2008) 092007.

[31] Varanda, M. J. on behalf of the Tilecal/ATLAS Collaboration. *The Tile Hadronic Calorimeter for the ATLAS Experiment*, LIP, Lisbon, Portugal.

[32] The ATLAS Muon Collaboration, *ATLAS Muon Spectrometer Technical Design Report*, (1997).

[33] Nave, Carl A. *Hyperphysics* URL site at:
http://hyperphysics.phy-astr.gsu.edu/hbase/nuclear/betaex.html. Copyright Nave 2006.

[34] Knoll, Glenn F. *Radiation Detection and Measurement. Third Edition*, Wiley Publication, Hoboken, New Jersey: 2000. P.357. ISBN 0-471-07338-5.

[35] S. Agostinelli, J. Allison, K. Amako, J. Apostolakis, H. Araujo, P. Arce, M. Asai, D. Axen, S. Banerjee, G. Barrand, F. Behner, L. Bellagamba, J. Boudreau, L. Broglia, A. Brunengo, H. Burkhardt, S. Chauvie, J. Chuma, R. Chytracek, and G. C. et al., *GEANT4 - a simulation toolkit*, Nuclear Instruments and Methods in Physics Research Section **A 506(3)** (2003).

[36] Geant4 Collaboration. URL Site at: http://geant4.web.cern.ch/geant4/ (2008).

[37] Garfield Collaboration. URL Site at: http://garfield.web.cern.ch/garfield (2008).

[38] ROOT: An Object-Oriented Data Analysis Framework, URL site at: http://root.cern.ch/, (2008).

[39] Maxwell: Electromagnetic Field Simulation for High-Performance Electromechanical Design. URL Site at: http://www.ansoft.com/products/em/maxwell (2008).

[40] FE-Desgin: Tosca Structure. URL Site at: http://www.fe-design.com/en/tosca/tosca.html (2008).

[41] Quickfield: A new Approach to Field Modelling. URL Site at: http://www.quickfield.com (2008).

[42] Femlab: The Unifying Multiphysics Simulation Environment. URL Site at: http://www.femlab.com (2008).

[43] Magboltz 7.1 Database. URL Site at: http://consult.cern.ch/writeup/magboltz/ (2008).

[44] Veenhof, Rob. *Choosing a gas mixture for the Alice TPC*, February 2003.

[45] Ramsauer, Carl. Unknown. *Ann. der Phys, Leipzig*, 66:546, 1921.

[46] Townsend, J. S. and Bailey, V. A. Unknown. *Phil. Mag*, 43:593, 1922.

[47] The ATLAS Muon Collaboration, Private Communication.

Acknowledgements

For the work on Neutrino Physics, I would like to thank everyone in the GERDA Collaboration at the Max Planck Institute in Munich. Specifically Prof. Dr. Allen Caldwell and Dr. Iris Abt who allowed me to work in the collaboration for three months. Also to all those who helped teach me so many invaluable lessons in European culture. Specifically, Kevin, Xiang, Franz, Manuela, Xing, Juraj, Bela, and Dano and Monika.

For the work at CERN, I would like to thank the IPP in Canada for the opportunity to work at CERN. Also, the entire Geant4 Collaboration for all their time and effort into getting my work started. Special thanks to Gabielle, John and Tanya. I would like to thank the whole of the SFT department whos doors were constantly being knocked on. And of course my supervisor Rob Veenhof for all of his patience on the work and time he took. I think I am almost ready to sail in a regatta.

Finally, I would like to thank the people who helped make this thesis possible, first of all to Lubka for her patience during the long nights. At the Universität Göttingen, Prof. Dr. Arnulf Quadt for allowing me this opportunity. I look forward to all the work ahead. Also to everyone in the High Energy Physics group for all their help. I'd like to thank Fabian and Kevin for their proofreading skills. A special thanks to Dr. Kevin Kröninger, who has always been there for questions and time even in the busiest times of the year. To think it still continues even long after the "Two meters tall long hair and a beard". Thank you to everyone.